

# Radiation driven winds from luminous accretion disks.

Daniel Proga<sup>a</sup>, James M. Stone<sup>b</sup>, and Janet E. Drew<sup>a</sup>

<sup>a</sup> *Imperial College of Science, Technology and Medicine, Blackett Laboratory, Prince Consort Road, London SW7 2BZ, UK*

<sup>b</sup> *Department of Astronomy, University of Maryland, College Park MD 20742, USA*

*E-mail: d.proga@ic.ac.uk, jstone@astro.umd.edu, and j.drew@ic.ac.uk*

12 October 2018

## ABSTRACT

We study the two-dimensional, time-dependent hydrodynamics of radiation-driven winds from luminous accretion disks in which the radiation force is mediated primarily by spectral lines. We assume the disk is flat, Keplerian, geometrically thin, and optically thick, radiating as an ensemble of blackbodies according to the  $\alpha$ -disk prescription. The effect of a radiant central star is included both in modifying the radial temperature profile of the disk, and in providing a contribution to the driving radiation field. Angle-adaptive integration techniques are needed to achieve an accurate representation of the driving force near the surface of the disk. Our hydrodynamic calculations use non-uniform grids to resolve both the subsonic acceleration zone near the disk, and the large-scale global structure of the supersonic wind.

We find that line-driven disk winds are produced only when the effective luminosity of the disk (i.e. the luminosity of the disk times the maximum value of the force multiplier associated with the line-driving force) exceeds the Eddington limit. If the dominant contribution to the total radiation field comes from the disk, then we find the outflow is intrinsically unsteady and characterised by large amplitude velocity and density fluctuations. Both infall and outflow can occur in different regions of the wind at the same time. The cause of this behaviour is the difference in the variation with height of the vertical components of gravity and radiation force: the former increases while the latter is nearly constant. On the other hand, if the total luminosity of the system is dominated by the central star, then the outflow is steady. In either case, we find the two-dimensional structure of the wind consists of a dense, slow outflow, typically confined to angles within  $\sim 45$  degrees of the equatorial plane, that is bounded on the polar side by a high-velocity, lower density stream. The flow geometry is controlled largely by the geometry of the radiation field – a brighter disk/star produces a more polar/equatorial wind. Global properties such as the total mass loss rate and terminal velocity depend more on the system luminosity and are insensitive to geometry. The mass loss rate is a strong function of the effective Eddington luminosity; less than one there is virtually no wind at all, whereas above one the mass loss rate in the wind scales with the effective Eddington luminosity as a power law with index 1.5. Matter is fed into the fast wind from within a few stellar radii of the central star.

Our solutions agree qualitatively with the kinematics of outflows in CV systems inferred from spectroscopic observations. We predict that low luminosity systems may display unsteady behavior in wind-formed spectral lines. Our study also has application to winds from active galactic nuclei and from high mass YSOs.

**Key words:** hydrodynamics – instabilities – methods:numerical – accretion discs – stars:mass-loss – cataclysmic variables

## 1 INTRODUCTION

Radiation-pressure driven wind models for main sequence and evolved OB stars developed over the past two decades have proven enormously successful in accounting for the

gross properties of such outflows. The essential concept underpinning these models is that momentum is extracted most efficiently from the radiation field via line opacity (Lucy & Solomon 1970; Castor, Abbott & Klein 1975, hereafter CAK). With the inclusion of lines, CAK showed that the effective radiation force can be increased by several

arXiv:astro-ph/9710305v1 27 Oct 1997

orders of magnitude above that due to electron-scattering alone, thus facilitating mass loss even from stars radiating at around 0.1% of their Eddington limit. A decade later it had become clear that the model was well able to predict time-averaged mass loss rates and terminal velocities in agreement with empirical estimates (Friend & Abbott 1986). More recently still, the goal has been to obtain a deeper understanding of instabilities inherent in the line-driving mechanism (e.g. Owocki, Castor & Rybicki 1988; Puls, Owocki & Fullerton 1993). These impressive achievements have all been set in the context of one-dimensional (spherical) geometry.

At the same time, accretion disks have come to be accepted as important components in a wide variety of astrophysical settings. These too can produce intense radiation fields at effective radiation temperatures comparable with those of OB stars. As an example, such disks are inferred from observations to be present in high state cataclysmic variables (CVs, see Warner 1995). Moreover, observations also show these same systems give rise to very high velocity winds that most probably emanate from deep within the gravitational potential in the vicinity of the accreting star (see Drew 1997). Another example of outflow associated with a luminous disk may be provided by higher mass YSOs (the BN-type objects and Herbig Be stars, see Mundt & Ray 1994 and references therein). In fact, in these objects it would not even be necessary to sustain a high mass accretion rate to achieve an intense radiation field – as one is already produced by the young OB star. Finally, shifting up the luminosity scale many orders of magnitude, the accretion disk model is now ‘standard’ for active galactic nuclei, and in this context as well, there is direct evidence of fast outflow in the broad absorption line (or BAL) QSOs (e.g. Weymann et al. 1991).

Given the success of one-dimensional models of line-driven winds from hot stars, it is natural to ask: what is the nature of line-driven winds from a star plus luminous accretion disk? In practice, calculating models for winds in disk systems is complex because of the intrinsically two-dimensional, axisymmetric character of the problem.

To render this problem amenable to analytic solution, previous studies have generally found it necessary to introduce simplifying or ad hoc assumptions. For example, in seeking a steady state accretion disk wind solution, Vitello & Shlosman (1988) found it necessary to enforce a radiation force term that increased with height above the disk and required a very particular variation in the ionization state of the gas – a matter that gave them cause for concern. More recently an analytic disk wind model has been designed by Murray *et al.* (1995) specifically for AGN. In order to simplify the problem they introduced heuristic assumptions which allowed the equations of motion in the radial and polar angle directions to be solved separately. Unfortunately, the outcome of their calculations depends in a basic way on these assumptions.

In this study, we face the multi-dimensional character of the disk wind problem directly, by adopting numerical meth-

ods to solve the dynamical equations from first principles. The first numerical treatment of the problem was formulated as long ago as 1980 (Icke 1980, see also Icke 1981). Icke (1980) set up what, in terms of today’s computing power, would now be regarded as a very modest calculation aimed at determining the character of an outflow from a disk driven by continuum (electron-scattering) radiation pressure only. In 1981 he incorporated rotation into his treatment and obtained results that we have found to be broadly comparable with our own as a partial test of our independent formulation. Like Icke, we choose a two-dimensional computational domain in which the central accreting object and inner disk are well-resolved. In our view this is important because of the evidence that disk winds in cataclysmic variables, a natural first test-bed for our results, originate close to the white dwarf. Recently Pereyra, Kallman & Blondin (1997, see also Pereyra 1997) have also presented numerical calculations of the two-dimensional structure of CV disk winds, albeit at a resolution too coarse to capture the inner disk structure or the subsonic portion of the outflow. Here, we use non-uniform meshes at high resolution to capture the structure of the wind in both the subsonic and supersonic regimes. Moreover, we employ a carefully-tested adaptive numerical integration technique to compute the line force directly within the Sobolov approximation. We make no restrictive geometric assumptions with regard to the flux integrals involved and show, on holding the force multiplier constant, that the line-driving force should be constant near the disk.

The original motivation for these calculations was to obtain self-consistent dynamical models for CV winds that remove the need to apply ad hoc kinematic structures in modelling observed ultraviolet spectral line profiles. Recent high quality observations obtained with the Hubble Space Telescope (e.g. Mason et al. 1995) have shown that the kinematic models designed for IUE data are already inadequate (Knigge & Drew 1997), and serve to emphasise the need for realistic rather than simplistic models.

Our models incorporate a star, for which we adopt the mass and radius appropriate to a white dwarf, and a geometrically thin accretion disk that is a source both of radiation and mass. In our formulation of the problem, the velocity field has three components that are functions of two spatial coordinates (sometimes referred to as a 2.5D formulation). For this reason, exact implementation of a force multiplier into the radiation force on spectral lines is formidable and some level of approximation required. We describe the formal solution of the problem and our approximations in section 2, with most of the analytic details given in appendices. We have developed numerical methods to compute both the radiation field from, and the radiation driving force, associated with the disk. These are coupled to the hydrodynamical code ZEUS-2D (Stone & Norman 1992). We describe our numerical methods and tests in section 3. Our particular interests are to explore the impact upon the mass loss rate and outflow geometry of (i) varying the system luminosity and (ii) varying the radiation field geometry by changing the relative contributions of the central star and disk radiation fields. Crudely speaking, we find that the mass loss rate is an extremely strong function of luminosity, while the

outflow geometry and its temporal behaviour are controlled by the radiation field's geometry. Some of our results have already been presented in a short communication (Proga, Drew & Stone 1997). A full description of our results is given in section 4. These are discussed together with their likely relevance and perceived limitations in section 5. The paper ends, in section 6, with our conclusions.

## 2 THE REPRESENTATION OF THE LINE DRIVING FORCE

To calculate the radiation force from a disk we need first to specify the disk's geometry and its radiation field. Consistent with existing conventions, we assume a flat, Keplerian, geometrically-thin and optically-thick disk. We calculate the disk radiation field from the surface brightness of the so-called  $\alpha$ -disk (Shakura & Sunyaev 1973). For models including a radiant central star, we take into account its irradiation of the disk, and assume that the disk re-emits all absorbed energy locally as a black body. The irradiation increases the disk temperature primarily in the inner part of the disk. In the presence of a luminous central star (CS), the disk temperature profile is altered such that the temperature decreases monotonically with radius, whereas a pure  $\alpha$ -disk is characterised by a temperature maximum at 1.36 stellar radii. See Appendix A for further details.

We approximate the radiative line force by means of the formalism introduced by CAK. A key assumption in their method is that the Sobolev approximation is valid, i.e. the radiation force exerted as a result of absorption of radiation coming from the central radiant object along a direction  $\hat{n}$  depends mainly on the velocity gradient along  $\hat{n}$ , at the point of absorption. CAK showed that for a spherically-expanding flow the radiation force due to a large ensemble of spectral lines can be expressed by

$$F^{rad,l} = F^{rad,e} M(t), \quad (1)$$

where  $F^{rad,e} = \frac{\sigma_e}{c} \mathcal{F}_*$ , is the radiation force due to electron scattering, and  $\mathcal{F}_*$  is the frequency integrated flux from the star. The quantity  $M$ , called the force multiplier, represents the increase in radiation force over the pure electron scattering case when lines are included. In the Sobolev approximation, it is a function of the optical depth parameter

$$t = \sigma_e \rho v_{th} \left| \frac{dv}{dr} \right|^{-1}, \quad (2)$$

where  $\rho$  is the density,  $v_{th}$  is the thermal velocity, and  $\frac{dv}{dr}$  is the velocity gradient along the radial direction (the only non-zero component in spherical symmetry). CAK found a fit to their numerical results for the force multiplier, such that

$$M(t) = kt^{-\alpha}, \quad (3)$$

where  $k$  and  $\alpha$  are parameters of the fit. They also showed that this expression for the force multiplier could be reproduced by assuming a simple statistical model of the distribution of lines in strength and frequency. This statistical model indicates that  $k$  is proportional to the total number of lines involved and  $\alpha$  is the ratio of optically-thick to optically-thin lines.

Subsequently the CAK formalism to approximate the radiation force due to lines has undergone a number of refinements (e.g., Abbott 1982; Pauldrach, Puls & Kudritzki 1986; Stevens & Kallman 1990, Gayley 1995). Many of the modifications are specific to 1D spherically-symmetric stellar winds. In this work we find the refinement introduced by Owocki, Castor and Rybicki (1988, OCR hereafter) is important. The formal specification of the force multiplier used by CAK allows an unlimited increase of the radiation line force with decreasing  $t$ , which is clearly unphysical (a point remarked upon by CAK). Instead one expects the force multiplier to saturate at some maximum value for very low  $t$  as all lines, including the most optically thick, contribute to the radiation force: a further decrease of  $t$  does not 'activate' any more lines. For example, this saturation can be seen in the radiation force calculations of Abbott (1982) in which he accounted for lines of the first to sixth stages of ionization of the elements H-Zn (see his figure 3). Generally he confirmed the CAK results. However his results showed that for  $t \lesssim 10^{-7}$ ,  $M(t)$  falls away from the CAK approximation (equation 3) as the force multiplier becomes less sensitive to  $t$ , the optical depth parameter. OCR considered this problem in terms of a line strength distribution. They modified the simple CAK statistical model by cutting off the maximum line strength and thereby limiting the effect of very strong lines:

$$M(t) = kt^{-\alpha} \left[ \frac{(1 + \tau_{max})^{(1-\alpha)} - 1}{\tau_{max}^{(1-\alpha)}} \right] \quad (4)$$

where  $\tau_{max} = t\eta_{max}$  and  $\eta_{max}$  is a parameter determining the maximum value,  $M_{max}$  achieved for the force multiplier. Equation (4) shows the following limiting behaviour:

$$\lim_{\tau_{max} \rightarrow \infty} M(t) = kt^{-\alpha} \quad (5)$$

$$\lim_{\tau_{max} \rightarrow 0} M(t) = M_{max}, \quad (6)$$

where  $M_{max} = k(1 - \alpha)\eta_{max}^\alpha$ . The maximum value of the force multiplier is in reality a function of physical parameters of the wind and radiation field. In a number of studies (CAK, Abbott 1982, Stevens & Kallman 1990, Gayley 1995) it has been shown that  $M_{max}$  is of the order of a few thousand.

To adapt the CAK formalism designed for OB stars to the disk wind case we need to accommodate two essential differences: (1) a stellar wind can be well approximated by a 1D radial flow while a disk wind is in general a 3D flow; (2) the stellar radiation field is spherically symmetric while the disk radiation is axially symmetric, as a consequence of

the disk geometry and the non-uniform disk intensity. First we consider the 3D nature of the flow. Rybicki & Hummer (1978, 1983) generalized the Sobolev method to the 3D case in which the flow velocity along a line of sight is not necessarily monotonic. In such a case, radiative coupling between distant parts of the flow must be taken into account. At this stage, where the flow properties are not known, we do not consider this effect. However, a further consequence of generalising the Sobolev method to 3 dimensions is that the Sobolev optical depth's dependence on the photon line-of-flight velocity gradient,  $|dv_l/dl|$ , may in practice become a complicated function of the velocity, velocity derivatives and position. In the generalized Sobolev method

$$t = t(\hat{n}, \mathbf{v}) = \frac{\sigma_e \rho v_{th}}{|dv_l/dl|}, \quad (7)$$

where the velocity gradient along the line of sight may be written

$$\frac{dv_l}{dl} = Q \equiv \sum_{i,j} \frac{1}{2} \left( \frac{\delta v_i}{\delta r_j} + \frac{\delta v_j}{\delta r_i} \right) n_i n_j = \sum_{i,j} e_{ij} n_i n_j \quad (8)$$

and  $e_{ij}$  is the symmetric rate-of-strain tensor. Expressions for the components of  $e_{ij}$  in the spherical polar coordinate system are given in Batchelor (1967). The complexity of the disk radiation field, together with the generalized optical depth parameter  $t$ , mean that the radiation line force at a given location due to the total radiating surface becomes a complicated integral in which the dependences on geometry, the radiation field and local optical depth are no longer separable.

For a 2.5D wind, we evaluate the disk radiation force in three steps. First, we calculate the radiation flux due to a surface element of the disk at a point above the disk,  $d\mathcal{F}_D$  (see Appendix A). Then we calculate the radiation force exerted by this flux via electron scattering,  $d\mathbf{F}_D^{rad,e} = \hat{n} \frac{\sigma_e}{c} d\mathcal{F}_D$ , and via an ensemble of lines  $d\mathbf{F}_D^{rad,l} = \hat{n} \frac{\sigma_e}{c} d\mathcal{F}_D M(t)$  (see Appendix B). Finally we integrate  $d\mathbf{F}_D^{rad,e}$  and  $d\mathbf{F}_D^{rad,l}$  over the total disk surface visible at the point in question (i.e., we exclude the disk region shadowed by the CS, see Appendix B). Our calculations of the radiation force contributed by the CS assume that it radiates as a blackbody at a fixed temperature and without any limb-darkening. We express the CS luminosity in alpha disk luminosity units  $x = L_*/L_D$ . The method of calculation of the radiation force from the CS is the same as for the disk, and takes into account disk occultation of the CS. In practice, evaluating the generalised optical depth (equation 7) using all terms in  $Q$  is computationally prohibitive. Instead, we keep only the dominant terms (see section 3.2 and Appendix C).

### 3 NUMERICAL METHODS

#### 3.1 Hydrodynamics

We use the 2D Eulerian finite difference code ZEUS-2D (Stone & Norman 1992) to calculate the wind structure. We have extended the code to include radiation forces due to electron scattering and line driving, i.e. we solve:

$$\frac{D\rho}{Dt} + \rho \nabla \cdot \mathbf{v} = 0, \quad (9)$$

$$\rho \frac{D\mathbf{v}}{Dt} = -\nabla(\rho c_s^2) + \rho \mathbf{g} + \rho \mathbf{F}^{rad} \quad (10)$$

where  $\mathbf{g}$  is the gravitational acceleration of the CS, and  $\mathbf{F}^{rad}$  is the total radiation force per unit mass. We describe how  $\mathbf{F}^{rad}$  is evaluated numerically in section 3.2. The gas in the wind is taken to be isothermal with a sound speed  $c_s$ .

Our calculations are performed in spherical polar coordinates  $(r, \theta, \phi)$  with  $r = 0$  at the centre of the accreting CS. We assume axial symmetry about the rotation axis of the accretion disk ( $\theta = 0^\circ$ ). Thus we assume that all quantities are invariant in  $\phi$ . Our standard computational domain is defined to occupy the radial range  $r_* \leq r \leq 10r_*$ , where  $r_*$  is the CS radius, and angular range  $0 \leq \theta \leq 90^\circ$  (in section 4.1 we compare the results to a solution computed on a grid ten times larger in radial extent, i.e.  $r_* \leq r \leq 100r_*$ ).

The  $r - \theta$  domain is discretized into zones. The gridding needs to be such as to ensure that the subsonic portion of the model outflow is sampled by at least a few grid points in both  $r$  and  $\theta$ . This requirement and the nature of the problem combine to demand an increasingly fine mesh toward the disk plane: here the density declines dramatically with height, and, moreover, the velocity in the wind increases rapidly. Our standard numerical resolution consists of 100 zones in each of the  $r$  and  $\theta$  directions, with fixed zone size ratios,  $dr_{k+1}/dr_k = d\theta_1/d\theta_{l+1} = 1.05$ . The smallest radial grid zone has dimension  $\Delta r_1 = 3.445 \times 10^{-3} r_*$  at  $r = r_*$ , while the smallest angular grid zone is  $\Delta \theta = 0.^\circ 029$  near  $\theta = 90^\circ$ . Gridding in this manner ensures good spatial resolution close to the radiating surfaces of the disk plane and the CS. In addition, to check that our solutions are resolved, we have computed the evolution of two of our models (our fiducial unsteady and steady wind cases – see sections 4.1 and 4.2 respectively) at twice this resolution, i.e. using 200 zones in each of the  $r$  and  $\theta$  directions, with  $dr_{k+1}/dr_k = d\theta_1/d\theta_{l+1} = 1.025$ . We find that the global properties of the solutions (such as the terminal velocity and mass loss rate) differ by no more than 10% between the high and standard resolution models.

The boundary conditions are specified as follows. At  $\theta = 0$ , we apply an axis-of-symmetry boundary condition. For the outer radial boundary, we apply an outflow boundary condition. For the inner radial boundary  $r = r_*$  and for  $\theta = 90^\circ$ , we apply reflecting boundary conditions.

The initial density profile is given by the condition of hydrostatic equilibrium in the latitudinal direction

$$\rho = \rho_0 \exp\left(-\frac{GM_*}{2c_s^2 r \tan^2 \theta}\right). \quad (11)$$

where  $\rho_0$  is the density in the first grid zone above the equatorial plane. Physically,  $\rho_0$  is analogous to the density in the photosphere of the disk at the base of the wind. The interior of the disk itself is treated as negligibly thin and is excluded from the models (for a disk temperature of  $10^4$  K at  $r = 2r_*$ , the disk scale height  $H$  is  $H/r_* \sim 10^{-3}$ ). The value chosen for  $\rho_0$  is arbitrary. Typically we choose  $\rho_0 = 10^{-9} \text{ g cm}^{-3}$ . As discussed in section 4.4, we find the gross properties of the winds are unaffected by the value of  $\rho_0$  provided it is large enough that the acceleration of the wind up to the sonic point is resolved with at least a few grid points. We set a lower limit to the density on the grid of  $\rho_{min} = 10^{-22} \text{ g cm}^{-3}$  and enforce it at all times in all models.

For the initial velocity field, we adopt  $v_r = v_\theta = 0$ , and  $v_\phi = \sqrt{\frac{GM_*}{r}}/\sin\theta$ . We find only the initial, transient evolution of the wind is affected by this choice of initial velocity conditions. At late times, we find all solutions for the same model parameter values have the same time-averaged properties regardless of the initial conditions. In order to represent steady conditions in the photosphere at the base of the wind, during the evolution of each model we continue to apply the constraints that in the first zone above the equatorial plane the radial velocity  $v_r = 0$ , the rotational velocity  $v_\phi$  remains Keplerian, and the density is fixed at  $\rho = \rho_0$  at all times. We have found that this technique when applied to calculations of spherically symmetric line-driven winds from stars, produces a solution that relaxes to the appropriate CAK solution within a few dynamical crossing times.

### 3.2 The radiation force

The integrals (Appendix B) that express the radiation force have to be evaluated numerically. To include the contribution from all radiating surface elements properly, the size of each surface element seen from a point W in the disk wind has to be in proportion to the distance from W to this surface element. In other words, the sampling should be uniform in apparent solid angle at W. A more subtle issue is that the vector character of the radiation force means that cancellation of opposing contributions to its net value can occur (e.g., in the radial component for points close to the disk plane). Care must therefore be taken in the numerical scheme that inappropriate gridding does not misrepresent such cancellations and thereby introduces spurious, fluctuating force terms. To satisfy both these important requirements we calculate the radiative force using grids of radiating surface elements that are adapted to every point W in the wind. The need to use adaptive integration methods is demonstrated by the tests discussed in section 3.3.

The integration scheme applied to the disk component of the radiation force uses a 2D version of Gaussian quadrature such that the number of quadrature points increases with increasing  $\theta$ . Because of foreshortening, the integrands (equations B3 and C7) are strong functions of the position on the disk plane for  $\theta$  close to  $90^\circ$  – they reach a maximum close to the point  $D_m$ ,  $(r_m, 90^\circ, 0^\circ)$ , wherein  $r_m$  is defined relative to  $r$  by  $n_r = 0$  for  $\theta = 90^\circ$  and  $\phi = 0^\circ$  (see Appendix A). Note that for  $\theta \lesssim 90^\circ$ , the point  $D_m$  is very close to the point on the disk for which the size of a surface element has to be the smallest (i.e.  $D_m$  lies close to the projection of W onto the disk plane). These properties of the integrands allow us to evaluate the radiation force accurately using a manageable number of grid points because the finest resolution on the disk plane is necessary mainly close to the point  $D_m$ . For the region far from  $D_m$ , we can afford less dense coverage of the disk surface.

In evaluating the integrals involved in the disk component of the radiation force (equations B3 and C7), we generally break the inner radial integral over  $(r_i, r_o)$  into two sub-integrals, spanning  $(r_i, r_m)$  and  $(r_m, r_o)$ . For cases where the point  $D_m$  falls within the inner, or beyond the outer, edge of the disk just the one integral over  $(r_i, r_o)$  is performed. The discretization of the disk surface uses 128, 256, 512, 1024 radial quadrature points for  $\theta \leq 87.^\circ 547$ ,  $87.^\circ 547 < \theta \leq 89.^\circ 518$ ,  $89.^\circ 518 < \theta \leq 89.^\circ 788$ , and  $\theta > 89.^\circ 788$ , respectively. We calculate the outer azimuthal integral over the angular range  $(0, \pi)$  with 128 and 512 quadrature points for  $\theta \leq 89.^\circ 002$  and  $\theta > 89.^\circ 002$ , respectively.

For the CS radiation force (equations B9 and C3), we use a 2D version of the trapezium method with the number of quadrature points increasing with decreasing  $r$ . In the polar direction, the stellar surface is divided up into 5000 and 500 grid points for  $r \leq 1.52r_*$  and  $r > 1.52r_*$  respectively. In the azimuthal direction, the resolution is 101 grid points for all  $r$ .

The evaluation of the line radiation force integrals is a major element in the computational cost of these simulations. The situation is exacerbated by the need to sample the subsonic part of the wind, close to the disk plane, reasonably well both in  $\theta$  and  $r$ . Indeed we find we cannot afford a full recalculation of the radiation line force for all locations, at every time step. Therefore we have to seek a working compromise between regular updating of the radiation line force and maintaining its accuracy in space. This suggests two contrasting ways of approximating the line force calculations: (1) the wind streamlines can be assumed to favour particular approximations to the velocity gradient that allow the radiation line force to be updated every time step; (2) the wind velocity can be assumed not to change rapidly with time at a given location, with the implication the line force need only be updated after some time interval taking into account the exact velocity vector.

The first approach amounts to a simplification of  $Q$  (equation 8) that enables the time-varying velocity gradient to be taken out of the integration over the radiating

surfaces. For present purposes, this is our preferred option and our particular implementation of it is presented in Appendix C. In physical terms, our treatment is equivalent to assuming that the transmission of disk light to points W in the wind will be controlled by the velocity shear in the vertical direction, and that the CS light has mainly to propagate through radial velocity shear. In specifying  $Q$ , this allows us to consider just  $dv_z/dz$  (where  $z$  is height above the disk plane) when computing the disk's contribution to the force and just  $dv_r/dr$  when calculating the CS component. This treatment should work well for the CS component throughout most of the computational domain and it should also be adequate for the disk component except, perhaps, close to the disk plane where neglect of the radial and azimuthal derivatives of the rotational component of motion ( $v_\phi$ ) will result in underestimation of the line force (i.e. inclusion of these terms would enhance  $Q$  for  $\theta \lesssim 90^\circ$ ). This neglect has less impact on the CS force component because foreshortening of the spherical stellar surface acts to reduce the weight of contributions from the larger angle, higher shear lines of sight with respect to the more nearly radial, low shear directions.

Within the present context in which unsteady flow has to be described, the second numerical approach of only updating the line force after a number of time steps requires more computational time. It does become both viable and accurate where the outflow achieves a steady state rather than a configuration that is steady only in a time-averaged sense. We are able to assess the impact of approximating  $Q$  upon our simulations in such cases. We return to this issue in section 4.4.

### 3.3 Tests of the numerical integration of the radiation force

The hydrodynamical algorithms implemented in the ZEUS-2D code have been extensively tested already (Stone & Norman 1992), thus here the primary concern is with tests of the integration of the radiative force term in the code. As a first check, we have tested that our numerical methods are able to reproduce the appropriate CAK wind solutions for spherically symmetric radiation fields. On the other hand, tests of fully multidimensional radiation fields are more difficult to construct. Thus our tests are restricted to the asymptotic behaviour of the electron-scattering component of the radiation force in a few cases where we know the analytical solution.

As  $\theta$  approaches  $90^\circ$ , we can treat the disk as an isothermal infinite plane. Therefore as  $\theta \rightarrow 90^\circ$  we expect the radial component of  $\mathbf{F}_D^{rad,e}$  to approach zero, while the latitudinal component of  $\mathbf{F}_D^{rad,e}$  becomes  $\theta$ -independent and equal to that exerted by the local disk flux. For high  $r$  and low  $\theta$ , the CS can be approximated by a point source. Thus the radial component of  $\mathbf{F}_*^{rad,e}$  should decrease there like  $r^{-2}$  and the latitudinal component of the radiation force should vanish. The radiation force calculated according to the numerical

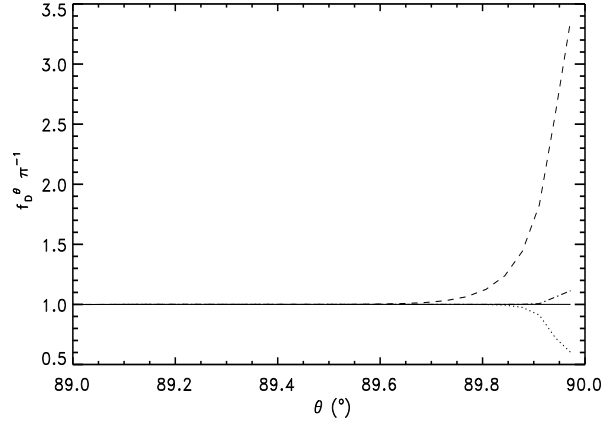


**Figure 1.** Numerical estimates of the vertical component of the geometric integral entering the radiation force for the isothermal disk case (equation 12). The results, normalised to the expected value of  $\pi$ , obtained for different numbers of grid points are shown. The solid line is obtained for 1024 adaptive grid elements, while the dashed-dotted, dotted, and dashed lines correspond respectively to estimates for 512, 256 and 128 quadrature points.

scheme described in §3.2 is a smooth function of  $r$  and  $\theta$ , and agrees with the above asymptotic solutions to within 5%. The discrepancy is attributable to fact that our disk is not isothermal – even for points close to the disk, regions of different temperature contribute to the force.

In the case that the disk is isothermal and without any CS irradiation ( $x = 0$ ), the  $\theta$ -component of equation B3 can be written as

$$f_D^\theta(r', \theta) = \int_{\phi_i}^{\phi_u} \int_{r'_i}^{r'_0} \frac{r'_D \cos \theta \cos \phi_D}{d'_D} \frac{r' \cos \theta}{d'_D{}^3} r'_D dr'_D d\phi_D. \quad (12)$$

For points very close to the disk plane and far from the disk edges the solution of equation 12 should be equal to  $\pi$ . Figure 1 illustrates how the numerical estimate of equation (12) depends on the number of grid points for  $r = 2r_*$ . As few as 128 quadrature points produces a satisfactory integral for points W at  $\theta \lesssim 89^\circ.5$ . For higher  $\theta$  however, only solutions based on 1024 quadrature points give an accurate estimate. Recall that in order to resolve the subsonic portion of the acceleration zone, we adopt a nonuniform grid with the smallest zones having an angular extent of only  $0.^\circ 029$ . Hence, there are many grid points in the region  $89^\circ.5 \leq \theta \leq 90^\circ.0$  where the use of densely-sampled adaptive quadratures is critical.

Before settling on the discretization described in §3.2 we tried using the trapezium method to integrate the radiation force due to the disk. To achieve as good agreement with the asymptotic solutions as obtained using the Gaussian scheme of §3.2, the trapezium method requires at least 2 orders of magnitude more grid points. We have also tried a modified version of the trapezium method using an exponential distribution of grid points around the point  $D_m$  – although this

**Table 1.** Full list of model parameters. The second column shows the parameters for model 2, while the third column indicates the parameter range explored for those parameters which we have varied.

Parameter	Value	Range
$M_*$	$0.6 M_\odot$	
$r_*$	$8.7 \times 10^8 \text{ cm}$	
$c_s$	$14 \text{ km s}^{-1}$	
$v_{th}$	$0.3 c_s$	
$\alpha$	0.6	0.4 – 0.8
$k$	0.2	
$M_{max}$	4400	
$\rho_0$	$10^{-9} \text{ g cm}^{-3}$	
$\rho_{min}$	$10^{-22} \text{ g cm}^{-3}$	
$\dot{M}_a$	$10^{-8} M_\odot \text{ yr}^{-1}$	$\pi \times 10^{-9}$ $– \pi \times 10^{-7} M_\odot \text{ yr}^{-1}$
$x$	0	0 – 10
$r_i$	$1 r_*$	
$r_o$	$10 r_*$	

method gave better results than uniformly distributed grid points, it remained inferior to Gaussian quadrature.

We have also experimented with the number of grid points used in calculating the radiation force due to the CS. This calculation is less demanding than that for the disk component. A reasonable number of grid points (as specified in §3.2) gives satisfactory agreement with the analytical solution for the asymptotic case.

## 4 RESULTS

Our numerical models are specified by a number of parameters. The CS is specified by its mass  $M_*$  and radius  $r_*$ . In all our calculations we assume  $M_* = 0.6 M_\odot$  which yields the CS radius  $r_* = 8.7 \times 10^8 \text{ cm}$  using the mass-radius relation for CO white dwarfs due to Hamada & Salpeter (1961). The accretion disk is characterized by the mass accretion rate through it,  $\dot{M}_a$  (which we treat as a free parameter), and by the sound speed  $c_s$  (fixed at  $14 \text{ km s}^{-1}$ ). Finally, the line-driving force is determined by the force multiplier parameters,  $k$ ,  $\alpha$ , and  $M_{max}$ , the maximum value allowed for the force multiplier, and by the thermal speed  $v_{th}$  which sets the line widths. As a starting point, we adopt typical OB star values for the force multiplier parameters,  $k$  and  $\alpha$  (i.e.  $k = 0.2$ ,  $\alpha = 0.6$ , see Gayley 1995), and subsequently vary  $\alpha$ . Tables 1 and 2 specify the parameter values of all the models discussed in sections 4.1, 4.2, and 4.3 below.

Our simulations suggest that there are two kinds of flow that might arise from luminous accretion disks (Proga, Drew, & Stone 1997). We describe a representative example of each of these two types of outflow in some detail first (sec-

tions 4.1 and 4.2). These are followed by a limited parameter survey in which we focus on the effects of varying three key parameters – the disk luminosity, the relative luminosity of the CS ( $x$ ) and the force multiplier index  $\alpha$ . Finally we draw attention to the role of some of the model assumptions in section 4.4.

### 4.1 A complex weak wind case

We begin the presentation of our results by describing the properties and behaviour of our model in which  $\dot{M}_a = 10^{-8} M_\odot \text{ yr}^{-1}$  and the central star is assumed to be dark ( $x = 0$ ). This is our model 2 (see Table 2).

Figure 2 presents a sequence of density maps and velocity fields (left and right hand panels) from model 2 plotted in the  $r, z$  plane. The figure displays the results of our high resolution ( $200 \times 200$  grid points) run. The length of the arrows in the right-hand panels is proportional to  $(v_r^2 + v_\theta^2)^{1/2}$ . The pattern of the direction of the arrows is an indication of the shape of the instantaneous streamlines. After  $\sim 10$  time units (we define the time unit as the orbital period at the surface of the CS,  $\tau = \sqrt{\frac{r_*^3}{GM_*}} = 2.88 \text{ sec}$ ) the disk material fills the grid for  $\theta \gtrsim 45^\circ$  and it remains in that region for the rest of the run. Figure 2 shows that the high density region usually corresponds to regions of low velocity. The variation in the orientation of the velocity arrows in the righthand panels indicates the flow is time-dependent and, moreover, it is clear that in some cases negative radial velocities (i.e. infall) are possible. The time dependence persists even after  $80 \tau$ . However it is important to note as discussed below that the gross properties of the flow (such as the mass loss rate), settle down to steady time-averages when averaged over timescales on the order of  $100 \text{ sec}$  ( $\sim 30\tau$ ) or more.

In model 2, the flow is complex with a few filaments sweeping outwards, typically, and various knots and clumps of gas moving both upwards and downwards. The direction and speed of motion at any one position is apt to change unpredictably with time; the velocity magnitudes at  $\theta > 60^\circ$  are typically less than  $\sim 100 \text{ km s}^{-1}$ . In the flow there is also a region where the material moves in a quite organized fashion. For  $45^\circ \lesssim \theta \lesssim 60^\circ$  beyond  $\sim 3r_*$  the material moves along nearly straight trajectories and leaves the outer boundary of the grid with velocities ranging from  $\sim 300$  up to  $\sim 1100 \text{ km s}^{-1}$ . However, at no location in even this part of the flow does the velocity ever exceed the local escape velocity (which decreases from  $4280 \text{ km s}^{-1}$  at  $r = r_*$  to  $1350 \text{ km s}^{-1}$  at  $r = 10r_*$ ). This does not mean that the mass loss will necessarily stall at a larger radius.

To investigate the nature of the outflow on larger scales, we have calculated this model on a computational domain that is ten times larger in the radial direction, i.e. it extends from  $r_*$  to  $100r_*$ . We use a grid of 100 angular zones and 150 radial zones for this model, so that the numerical resolution in the inner region of the grid (i.e.  $r \leq 10r_*$ ) is identical to

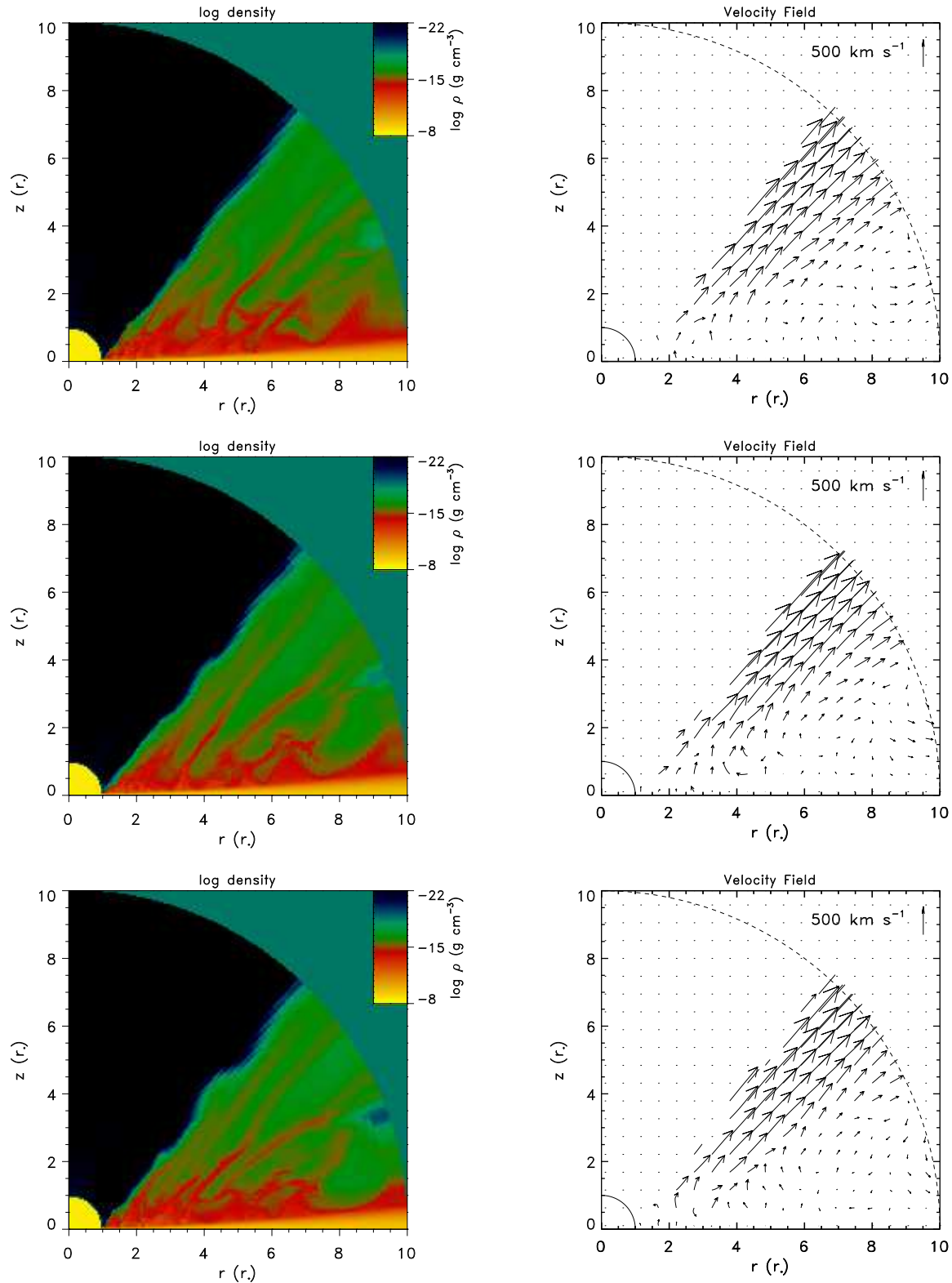


**Figure 2.** A sequence of density maps (left) and velocity fields (right) from run 2 after 208, 226 and 239  $\tau$  (upper, middle and lower panels). Run 2 is the example of unsteady flow discussed in detail in section 4.1. Note the time-dependent fine structure in density and changing velocity vectors at polar angles greater than  $\sim 65^\circ$ .



**Table 2.** Summary of parameter survey.

Run	$\alpha$	$\dot{M}_a$ ( $M_\odot \text{ yr}^{-1}$ )	$x$	$\dot{M}_w$ ( $M_\odot \text{ yr}^{-1}$ )	$v_r(10r_*)$ ( $\text{km s}^{-1}$ )	comments
1	0.6	$\pi \times 10^{-9}$	0			no supersonic outflow
2	0.6	$10^{-8}$	0	$4.8 \times 10^{-14}$	900	fiducial complex wind (see §4.1)
3	0.6	$\pi \times 10^{-8}$	0	$4.7 \times 10^{-12}$	3500	complex wind
4	0.6	$10^{-7}$	0	$4.0 \times 10^{-11}$	4500	complex wind
5	0.6	$\pi \times 10^{-7}$	0	$3.1 \times 10^{-10}$	7500	complex wind
6	0.6	$\pi \times 10^{-9}$	1			no supersonic outflow
7	0.6	$10^{-8}$	1	$1.3 \times 10^{-12}$	2000	complex wind
8	0.6	$\pi \times 10^{-8}$	1	$1.2 \times 10^{-11}$	3500	fiducial steady outflow (see §4.2)
9	0.6	$10^{-7}$	1	$1.5 \times 10^{-10}$	6000	steady state
10	0.6	$\pi \times 10^{-9}$	3	$4.7 \times 10^{-13}$	1200	weakly time-variable
11	0.6	$10^{-8}$	3	$6.0 \times 10^{-12}$	3500	steady state
12	0.6	$\pi \times 10^{-8}$	3	$4.7 \times 10^{-11}$	5000	steady state
13	0.6	$10^{-7}$	3	$3.5 \times 10^{-10}$	7000	steady state
14	0.6	$\pi \times 10^{-8}$	10	$3.1 \times 10^{-10}$	7000	steady state
15	0.4	$\pi \times 10^{-8}$	0	$6.2 \times 10^{-15}$	3000	complex wind
16	0.4	$10^{-7}$	0	$1.6 \times 10^{-13}$	6000	complex wind
17	0.8	$\pi \times 10^{-8}$	0	$6.2 \times 10^{-11}$	2500	complex wind
18	0.8	$10^{-7}$	0	$6.3 \times 10^{-10}$	7500	complex wind
19	0.8	$\pi \times 10^{-7}$	0	$4.0 \times 10^{-9}$	14000	complex wind

our standard case. The results of this calculation show that the integrated mass loss rate at  $100r_*$  is the same as that at  $10r_*$ . Moreover, the fast stream does continue to accelerate beyond  $10r_*$ , so that  $v_r$  rises from  $\sim 1100 \text{ km s}^{-1}$  at  $10r_*$  up to  $1300 \text{ km s}^{-1}$  or so at  $100r_*$  (which is well above the escape velocity at this point). That the fast outflow eventually exceeds escape velocity is not surprising since at large radii the density of the flow is so low that the radiation force reaches its maximum value set by  $M_{max}$ : thus both gravity and the radiation force will scale with radius as  $r^{-2}$ . Consequently, not only can the total force never change sign (because the ratio of the radiation force to gravity is constant), but also the total force decreases in magnitude rapidly, so that the flow velocity no longer changes significantly. More importantly, the model on the larger grid indicates the mass loss is completely dominated by material arising from the inner ( $r < 10r_*$ ) region of the disk.

Next we consider the time and angle dependence of the gross properties of the flow at large radii. Figure 3 is a plot of the angular dependence of density, radial velocity, mass flux density, and accumulated mass loss rate at  $r = r_o = 10r_*$  at the same times as Figure 2. The accumulated mass loss rate is given by:

$$d\dot{m}(\theta) = 4\pi r_o^2 \int_{0^\circ}^{\theta} \rho v_r \sin \theta d\theta. \quad (13)$$

The gas density is a very strong function of angle for  $\theta$  between  $\sim 90^\circ$  and  $45^\circ$ . Between the disk mid-plane at  $\theta = 90^\circ$  and  $\theta \sim 85^\circ$ ,  $\rho$  drops by  $\gtrsim 6$  orders of magnitude, as might be expected of a density profile determined by hydrostatic equilibrium (see equation 11). For  $45^\circ \lesssim \theta \lesssim 85^\circ$ , the wind domain,  $\rho$  varies between  $10^{-17}$  and  $10^{-15} \text{ g cm}^{-3}$ . For  $\theta \lesssim 45^\circ$ , density again decreases exponentially, but this time to so low a value that it becomes necessary to replace it by the numerical lower limit  $\rho_{min}$ . The region with  $\rho \leq \rho_{min}$  is not relevant to our analysis as it has no effect on the disk flow. The radial velocity at  $10r_*$  varies around zero with an amplitude  $\lesssim 100 \text{ km s}^{-1}$  for  $65^\circ \lesssim \theta \lesssim 90^\circ$ . Over the angular range  $65^\circ > \theta > 45^\circ$ ,  $v_r$  increases from  $\leq 100$  up to  $1200 \text{ km s}^{-1}$ .

The cumulative mass loss rate is negligible for  $\theta \lesssim 45^\circ$  because of the very low prevailing gas density. Beginning at  $\theta \gtrsim 45^\circ$ ,  $d\dot{m}$  increases to  $\sim 4 \times 10^{12} \text{ g s}^{-1}$  at  $\theta \approx 83^\circ$ . Then, in the region close to the disk plane, where the gas density starts to rise very sharply and where the motion is typically more complex, the cumulative mass loss rate is subject to enormous fluctuations (some of which may even be negative!). In the example shown as figure 3, the total mass loss rate through the outer boundary,  $\dot{M}_{tot} = d\dot{m}(90^\circ)$  reaches  $\sim 5 \times 10^{13} \text{ g s}^{-1}$ . This figure is most certainly dominated by the contribution from the slow-moving region very close to the disk mid-plane – a contribution that is very markedly time-dependent.

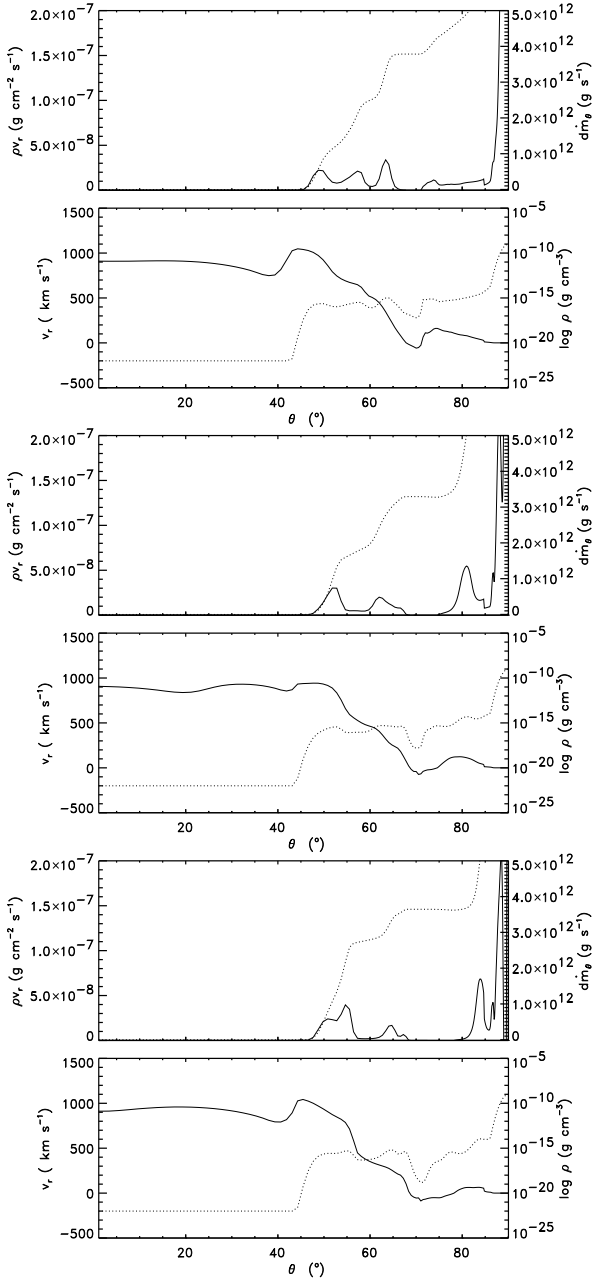


**Figure 3.** A sequence showing how quantities at the outer boundary in model 2 change as a function of time. As in Figure 2 the top, middle and lower panel pairs refer to the times 208, 226 and 239  $\tau$ . In each panel the ordinate on the left hand side describes the solid line, while the ordinate on the right hand side refers to the dotted line. All curves show considerable structure that is time-variable. The cumulative function  $d\dot{m}(\theta)$  (dotted line, upper panel in each pair) is smoother and less variable, illustrative of the manner in which global quantities tend toward steady time averages.

To provide some insight into the time dependence, figure 4 shows the time evolution of volume-averaged quantities for run 2. The total mass on the grid,  $M_{tot}$ , is subject only to small changes. It increases by  $\sim 1\%$  during the first 60  $\tau$ , and then decreases again, dropping back to 1.006 of the initial value,  $M_{tot}(0)$ , by 170  $\tau$ . After this time  $M_{tot}$  starts to fluctuate between  $\sim 1.006 M_{tot}(0)$  and  $\sim 1.01 M_{tot}(0)$ . By con-

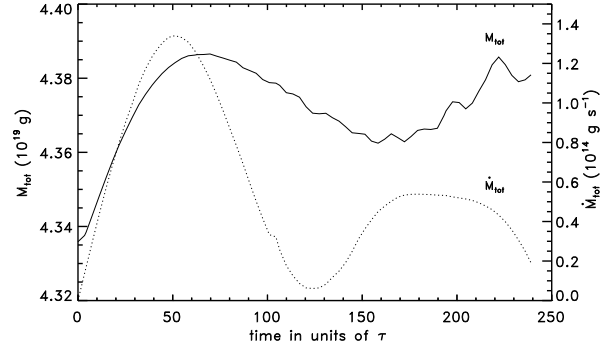


**Figure 4.** The time evolution of the total mass on the grid and the total mass loss rate ( $d\dot{m}(90^\circ)$ ) for model 2. The strong modulation of the total mass loss rate is dominated by the slow and highly variable flow component close to the disk plane (see figures 2 and 3). In this case, the relatively steady fast stream at  $\theta \sim 65^\circ$  contributes only  $\sim 10\%$  of the total mass loss.

trast, the total mass loss rate is seemingly a strong function of time. Initially, it rises steeply, peaking at  $1.3 \times 10^{14} \text{ g s}^{-1}$  at 50  $\tau$ . Then it plummets to  $5 \times 10^{12} \text{ g s}^{-1}$  at  $\sim 120\tau$  and starts oscillating with decreasing amplitude. These large swings are entirely a consequence of the complex character of the flow close to the disk mid-plane. A much steadier, and consistently positive, cumulative mass loss rate is achieved if the integration over polar angle is stopped at  $\theta \lesssim 70^\circ$  (see figure 3). A further justification for stopping the integration at this angle, is that  $d\dot{m}$  is then the mass loss rate associated with just the hypersonic outflow that easily escapes the system.

## 4.2 A strong steady outflow model

We find that unsteady outflow such as that described above in section 4.1 persists as long as the disk radiation field is dominant (small  $x$  in our parameterisation). However, as the radial component of the radiation field is increased with respect to the latitudinal ( $\theta$ ) component, by adding in light from a central star (CS), we find that the volume occupied by unsteady outflow diminishes. Indeed, in the presence of a strong radiation force due to the CS, a disk wind can even settle into a steady state.

Model 8 is a contrasting example of a strong outflow in a steady state. In it, we set the CS luminosity equal to the intrinsic disk luminosity (i.e.  $x = 1$ ), and chose  $\dot{M}_a = \pi \times 10^{-8} M_\odot \text{ yr}^{-1}$ . The remaining model parameters and the initial conditions are as specified in Tables 1 and 2. Figure 5 is the density map and velocity field for this model after 240 $\tau$ . The flow is almost in a steady state by then, with the gas density a smooth function of position. The flow may be described as organized and regular. Small changes with time still occur, but only very close to the disk plane.

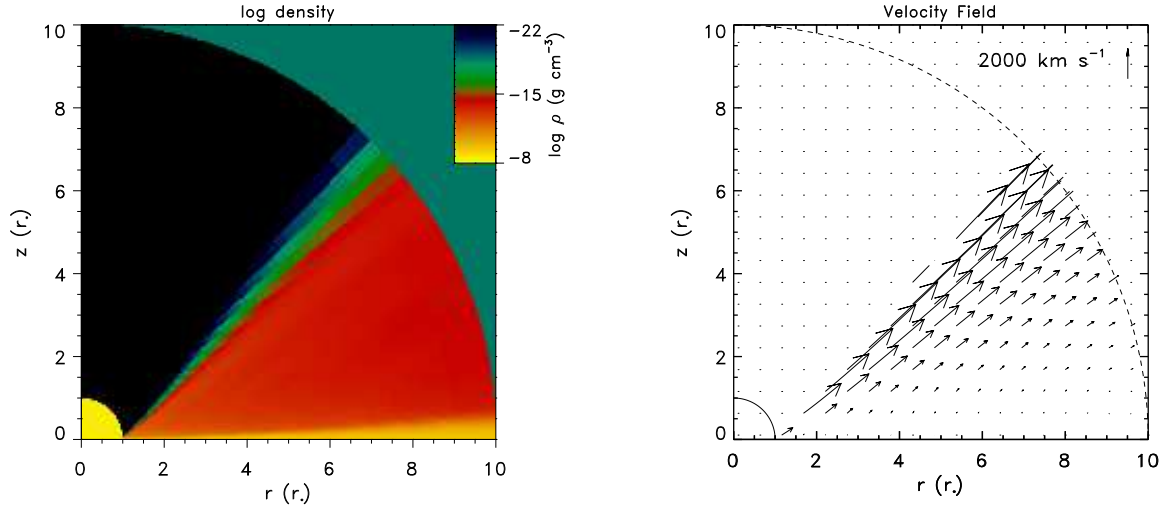


**Figure 5.** The density map and velocity field for model 8 after  $240 \tau$ . Note the absence of fine structure in the density map and the regularity of the velocity field.

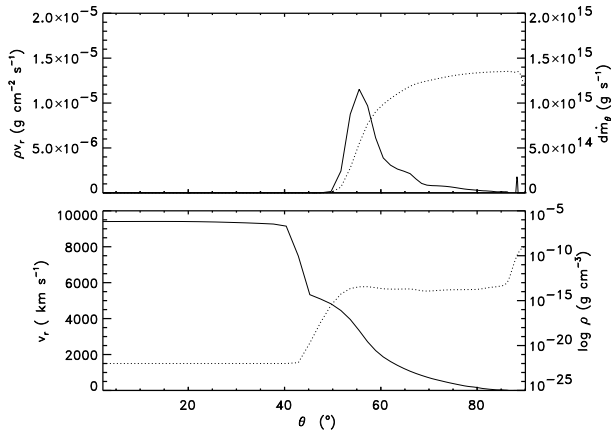


**Figure 6.** Quantities at the outer boundary in model 8 after  $240 \tau$ . The ordinate on the left hand side of each panel refers to the solid line, while the ordinate on the right hand side refers to the dotted line. Of particular note is the pronounced  $\rho v_r$  peak at  $\theta \sim 55^\circ$ . This is associated with the fast stream that contributes  $\sim 90\%$  or so of the total mass loss.

Figure 6 presents the wind properties as function of  $\theta$  at  $r = 10r_*$  after  $240\tau$ . On this surface, the flow density varies between  $10^{-14}$  and  $10^{-13} \text{ g cm}^{-3}$  for  $50^\circ \leq \theta \leq 85^\circ$ . Within the same  $\theta$  range,  $v_r$  increases from low values on the order of  $100 \text{ km s}^{-1}$ , up to  $\sim 4000 \text{ km s}^{-1}$  as  $\theta$  decreases. The accumulated mass loss rate is  $1.3 \times 10^{15} \text{ g s}^{-1}$  at  $\theta \sim 80^\circ$ . This is a factor of  $\sim 400$  increase with respect to the mass loss rate obtained in model 2, for just a factor of  $2\pi$  increase in total luminosity.

Figure 7 shows the time evolution of volume-averaged quantities in model 8. This should be contrasted with the equivalent figure for model 2 (figure 4). As in model 2 all the quantities plotted are subject to fluctuations of the wind

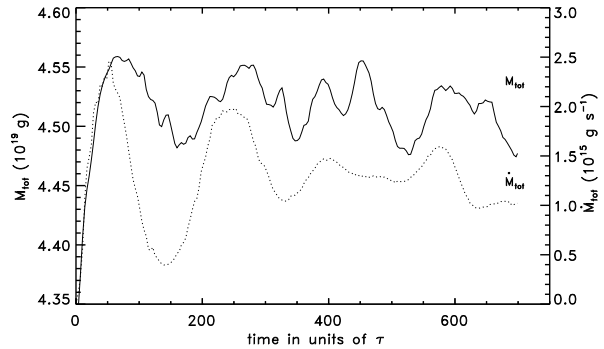


**Figure 7.** The time evolution of the volume-averaged quantities for model 8 (to be compared with model 2 shown in figure 4). In this case the total mass loss rate is much more settled, reflecting a very nearly steady flow and the dominant role of the fast stream at  $\theta \sim 55^\circ$ .

properties near the disk plane, where the flow does not quite settle into a steady state. However the magnitude of these fluctuations of the total mass loss rate has collapsed from a factor of 10 (model 2, figure 4) to around 1.5 (model 8, figure 7).

### 4.3 Parameter survey

As is fitting for a first exploration of radiation-driven wind models from disks, we aim to examine only the parameter space of our models that will define the major trends in disk wind behaviour. Table 2 lists the models considered. We em-

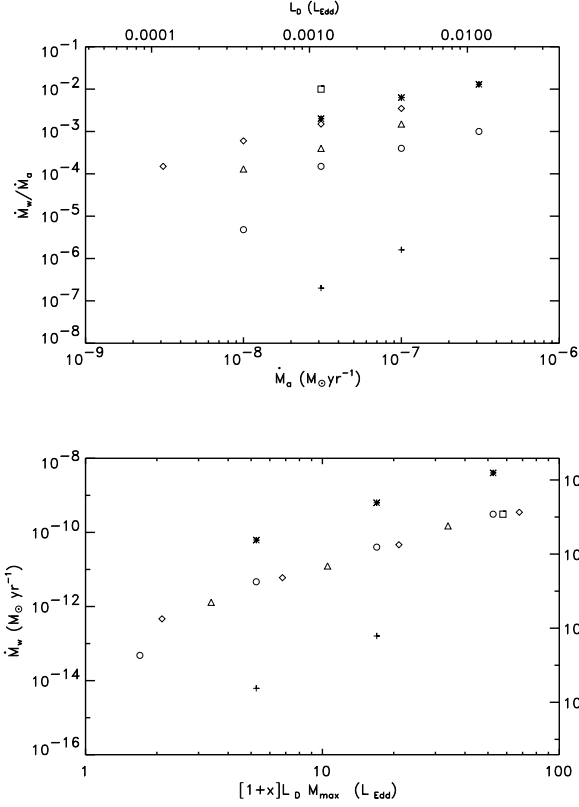


**Figure 8.** Model mass loss rates as functions of the mass accretion rate (top panel) and effective total luminosity in units of the Eddington luminosity (bottom panel). All open symbols are for models with  $\alpha = 0.6$ , the different shapes corresponding to different  $x$  ( $x = 0$  circles,  $x = 1$  triangles,  $x = 3$  diamonds,  $x = 10$ , squares). The crosses represent models for  $\alpha = 0.4$  and  $x = 0$  while stars represent models for  $\alpha = 0.8$  and  $x = 0$ . Tables 1 and 2 specify all other model parameters. The alternative ordinate on the right hand side of the lower panel is the dimensionless wind mass loss rate parameter  $\dot{M}'_w$  defined in equation 22, section 5.3.

phases a survey of how the mass loss rate, outflow velocity and geometry change with disk luminosity and relative CS luminosity. In view of the important formal role that the force multiplier index  $\alpha$  is known to play in determining one-dimensional stellar wind solutions (i.e.  $\dot{M}_w \propto L^{1/\alpha}$ ), we have also calculated a few models in which the index  $\alpha$  been set equal to the relatively extreme values of 0.4 and 0.8 (see Gayley 1995). So that we might focus on this dependence, we arbitrarily hold  $k$  and  $M_{max}$  constant.

In Figure 8 we show (a) the derived ratio,  $\dot{M}_w/\dot{M}_a$ , as a function of  $\dot{M}_a$  and (b) the wind mass loss rate,  $\dot{M}_w$ , as a function of the total effective luminosity,  $[1+x]L_D M_{max}$ , for various  $x$  and  $\alpha$ . We define  $\dot{M}_w$  as the cumulative mass loss rate for the region well above the disk plane in which the highly supersonic, organized flow is located (i.e. the angular integral is stopped early enough to avoid the exponential density profile of the disk and any lower-velocity complex flow component at  $\theta$  near  $90^\circ$ ). The total effective luminosity is the total luminosity of the system,  $[1+x]L_D$ , multiplied by the maximum value of the force multiplier  $M_{max}$  (see the discussion leading to equation 4); it is measured in Figure 8

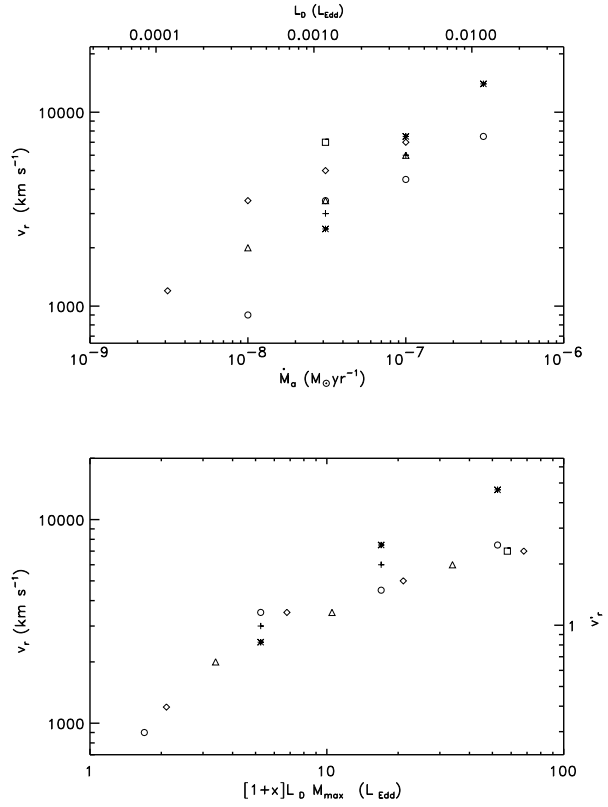


**Figure 9.** Typical fast stream velocities at the outer boundary ( $r = 10r_*$ ) for all models as functions of the mass accretion rate (top panel) and effective total luminosity in units of the Eddington luminosity. All symbols have the same meaning as in figure 8. The alternative ordinate on the right hand side of the lower panel is the dimensionless velocity parameter  $v'$  defined via equation 17 in section 5.3.

in units of the classical Eddington value. In Figure 8a it can be seen that  $\dot{M}_w/\dot{M}_a$  is a very strong function of  $\dot{M}_a$  for  $x = 0$ . At low  $\dot{M}_a$  there is virtually no disk wind at all. The outflow turns on sharply for  $\dot{M}_w \gtrsim 10^{-8} M_\odot \text{yr}^{-1}$ , and then there is a flattening out of  $\dot{M}_w/\dot{M}_a$  to follow a power law of index  $\sim 1.5$  for  $\dot{M}_w \gtrsim \pi \times 10^{-8} M_\odot \text{yr}^{-1}$ . A similar trend is apparent from the  $x = 1$  and  $x = 3$  models, with the difference that increased  $x$  at a fixed mass accretion rate  $\dot{M}_a$  results in a higher mass loss rate. But when, instead, the absolute values of the calculated mass loss rates are considered just as a function of the total effective luminosity, this family of curves for different  $x$  collapses, most impressively, into a single curve. This is shown in Figure 8b. That this occurs shows that  $\dot{M}_w$  is not itself sensitive to the geometry of the driving radiation field (provided that  $L_D M_{max}$  is higher than the Eddington limit). A further point to note from Figure 8b is that a disk together with CS will produce a fast wind for  $\alpha = 0.6$  if the effective luminosity is higher than  $\sim 2$  times the Eddington limit.

Our models for  $\alpha = 0.4$  and 0.8 indicate that the wind mass loss rate is very sensitive to the rapidity with which the force multiplier saturates at its maximum value (i.e. the limit in which all lines have become optically-thin). For  $\alpha = 0.8$ ,  $\dot{M}_w$  is  $\sim 4$  orders of magnitude higher than for  $\alpha = 0.4$ .

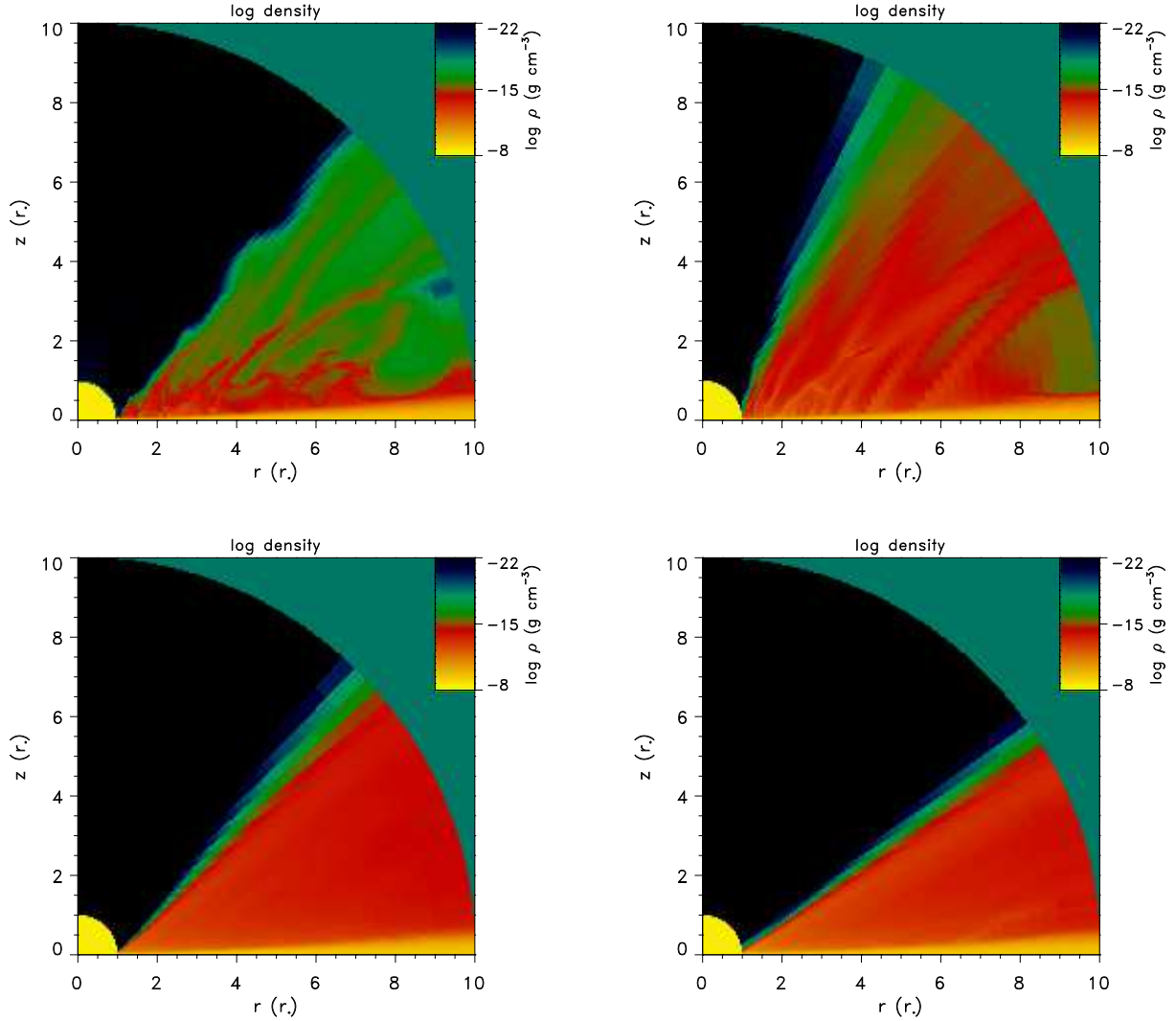


**Figure 10.** The top two panels, a and b, are density maps for models with  $x = 0$  and  $\dot{M}_a = 10^{-8} M_\odot \text{yr}^{-1}$  (model 2) and  $\dot{M}_a = \pi \times 10^{-8} M_\odot \text{yr}^{-1}$  (model 3). The bottom two panels, c and d, are density maps for models with  $\dot{M}_a = \pi \times 10^{-8} M_\odot \text{yr}^{-1}$  and  $x = 1$  (model 8) and  $x = 3$  (model 12). The top two panels show the effect on the outflow geometry of increasing the disk luminosity alone, while the top right and bottom two panels show the effect in an increasingly larger stellar component ( $x = 0, 1$  and  $3$ ) to the radiation field. The stronger the disk radiation field the more polar the flow becomes. Adding in an increasingly large stellar component causes the outflow to become more equatorial.

Higher  $\alpha$  yielding higher mass loss simply reflects the fact that the force multiplier is higher for a given  $t$  (where  $t$  is the optical depth parameter defined in equation 7). The extremity of the effect shows that it does not require large shifts in the relative magnitudes of the radiation force and effective gravity to make the difference between negligible and efficient mass loss. Interestingly, there seems to be no change in the power law dependence of  $\dot{M}_w$  on luminosity between  $\alpha = 0.6$  and  $\alpha = 0.8$ , in contrast to the behaviour of one-dimensional stellar wind solutions.

Figure 9 presents how the wind radial velocity at  $10r_*$  changes with  $\dot{M}_a$  and  $[1+x]L_D M_{max}$  for various  $\alpha$ . The figure we quote is  $v_r$  of the gas at a representative angle in

the supersonic part of the outflow – this is usually  $v_r$  at the polar angle where  $\rho v_r$  peaks in the fast stream (see Figure 3). Generally, the wind velocity is a weaker function of the disk luminosity than  $\dot{M}_w$ . Figure 9b suggests that  $v_r$  increases with  $[1+x]L_D M_{max}$  along one universal curve at fixed  $\alpha$ , mirroring the single relation found also for the mass loss rate. This curve is not as smooth as that for  $\dot{M}_w$  because of inherent imprecision in our method of determining  $v_r$ . The radial velocity is a strong function of  $\theta$  and also may change with time. To obtain a smoother curve we would have had to calculate many of our models for longer and then derive a consistent set of time averages rather than make ‘by eye’ measurements as here. Despite this, the trend is clear enough that  $v_r$  scales with  $[1+x]L_D M_{max}$  in our wind models.

While it is true of our models that the integrated mass loss rate and typical radial outflow velocity are not sensitive to the particular geometry of the radiation field, this does not mean that the radiation geometry has no role to play. Panels b, c and d of Figure 10 compare the flow pattern from three models in which the mass accretion rate (and therefore disk luminosity) is held fixed at  $\dot{M}_a = \pi \times 10^{-8} M_\odot \text{ yr}^{-1}$  and the luminosity of the central star is varied using  $x = 0, 1,$  and  $3$ . Note this implies that the total luminosity (disk plus star) is increasing. It can be seen that, as the contribution of the central star to the radiation field grows, the flow becomes more equatorial. This is unsurprising given that the increasing contribution from the central star boosts the radial component of the radiation force, while contributing little to the (negative)  $\theta$  component.

However, it is important to realise that the flow geometry also responds, for a fixed radiation geometry, to a change in the driving luminosity. Panels a and b of Figure 10 compare the flow pattern from two models in which the mass accretion rate (and therefore disk luminosity) is changed from  $\dot{M}_a = 10^{-8} M_\odot \text{ yr}^{-1}$  to  $\dot{M}_a = \pi \times 10^{-8} M_\odot \text{ yr}^{-1}$ , while the central star is assumed to be dark, i.e.  $x = 0$ . The contrast between these two panels shows how a more luminous disk will power a stronger, more vertically-directed wind. Specifically, an increase of a factor  $\pi$  in the mass accretion rate is sufficient to divert the fast boundary stream from  $\theta \sim 45^\circ$  to  $\theta \sim 30^\circ$ .

#### 4.4 Sensitivity of models to assumptions

There are two parameters in our models listed in Table 1 whose values seem arbitrary, yet which may appear important in determining our solutions. These are the density at the base of the wind  $\rho_0$  and the maximum value of the force multiplier  $M_{max}$ . In this section, we discuss the effect on our models of varying these parameters. We also discuss the tests we have performed of the sensitivity of our solutions to the approximations made in calculating the line-driving.

First, we consider the effect of varying  $M_{max}$ . In principle,  $M_{max}$  is a function of  $k$ ,  $\alpha$  and  $\eta_{max}$  (cf. equation 6). In this paper, we have treated  $k$  and  $\alpha$  as free parameters and studied the effect of varying  $\alpha$  in section 4.3. In this case,  $\eta_{max}$  was also varied to keep  $M_{max}$  fixed. Instead, here we investigate the effect of varying  $\eta_{max}$  (and therefore  $M_{max}$ ) for fixed  $k$  and  $\alpha$ . As pointed out in section 2,  $M_{max}$  is not an arbitrary quantity, but we expect it only to take effect in regions where the optical depth  $t$  is small. Since  $\dot{M}_W$  is likely to be fixed near the wind base in the higher  $t$  domain, we may anticipate that moderate changes in  $\eta_{max}$  ( $M_{max}$ ) are more likely to have a bearing on the strongly supersonic flow and alter, for example, the wind terminal velocity. Our tests indicate this is the case. Of course very low  $\eta_{max}$  ( $M_{max}$ ) can adversely affect the driving near the base of the flow and, if low enough, quench the wind altogether. If we treat  $M_{max}$  as the parameter identifying the scale of the line driv-

ing force, we can use it to set the following rough lower limit on the total luminosity needed to produce a fast disk wind:

$$(1+x)L_D \gtrsim L_{Edd}/M_{max}, \quad (14)$$

where  $L_{Edd} = \frac{4\pi cG}{\sigma_e} M_*$  is the Eddington luminosity.

Next, we consider the effect of varying the density  $\rho_0$  at the base of the wind. The radiation force due to lines per unit mass is a function of gas density (equations 2–4) such that the higher the density, the lower the force. For  $\theta$  near  $90^\circ$ , the total force acting on the gas is nearly equal to the radiation force since the effective gravity near the disk midplane is small. In this region, therefore, the boundary density  $\rho_0$  controls not only the radiation line force but also the total force acting on the gas. We have tested the sensitivity of our model winds to changes in our assumed value for  $\rho_0$ . We find that for  $\rho_0 \gtrsim 10^{-10} \text{ g cm}^{-3}$ , the flow is transsonic (i.e. the subsonic portion of the flow is resolved on our numerical mesh), and the properties of the outflow do not depend on the value of  $\rho_0$ . On the other hand, for  $\rho_0 < 10^{-10} \text{ g cm}^{-3}$  the line radiation force per unit mass is high at the outset, giving rise to a steady supersonic outflow even at the wind base (i.e. the flow becomes supersonic in less than one grid point). This is clearly unphysical: if the radiation force per unit mass were this high in a real disk, subsonic outflow would have begun at much higher densities deeper in the disk.

The highest allowed value for the density at the base of the wind must be less than the density at the midplane of the disk. In principle, the density along the disk plane can be determined self-consistently from disk structure models. At the same time, the density at the base of the wind must be large enough to produce a transsonic wind. Disk structure models have shown that the density in the disk midplane is  $\gtrsim 10^{-9} \text{ g cm}^{-3}$  (e.g. Pringle 1981, Carroll *et al.* 1985), thus the value  $\rho_0 = 10^{-9} \text{ g cm}^{-3}$  we adopt in our models can be seen to be entirely satisfactory.

Finally, we have also examined the sensitivity of our solutions to the assumptions we adopt to compute the line driving force (see Appendix C). While it is infeasible to evaluate the generalized CAK force in our models at every timestep, it is feasible to evaluate it at a particular time for all locations in the flow, in order to compare the exact calculation with the force computed approximately. Typically, we find the biggest discrepancies very close to the disk surface: the full treatment of the generalized force yields an acceleration up to an order of magnitude higher than that given by our approximation. This is because of the extra contributions from terms depending on  $v_\phi$  in the rate of strain tensor which we drop. However, as the flow is accelerated, these terms are quickly overwhelmed by terms which depend on  $v_z$  and  $v_r$  that are included in our approximations. Thus, a few degrees above the surface of the disk, our approximate form for the radiation force is in good agreement with the full expression. Moreover, as the optical depth in the lines decreases, the force reaches its maximum value  $M_{max}$

and becomes independent of the approximations we adopt. Typically the force saturates at just a few stellar radii in response to the declining wind density.

Still, it is possible that the increased radiation force close to the disk plane in a more exact treatment may affect the solutions by, e.g., increasing the mass loss rate in the wind for a given disk luminosity. Thus, the development of an efficient computational scheme that can relax to a hydrodynamical solution consistent with the full form of the generalized line-driving force is important: we will present such results in a future communication. However, the current tests of our approximations give no indication that the key features of our results (the unsteady nature of radiation driven disk winds, or the overall two-dimensional geometry of such winds) are sensitive to an improved representation of the radiation force.

## 5 DISCUSSION

### 5.1 Origin of unsteady outflow

The most dramatic result of these models is the discovery of unsteady outflow in many of the cases that we have considered. This component when present occurs in the base of the outflow near the disk. It is characterised by large amplitude density and velocity variations. It is important to ask what is the origin of this behaviour. We identify several factors which contribute to it.

The first, and fundamental driver of the behaviour, is the difference in the height dependence of the vertical components of gravity and the radiation force. The former increases linearly whilst the flux integral central to the latter is nearly constant in the brightest parts of the disk. The consequence is that mass lifted off the disk plane by radiation pressure is susceptible to stalling as the increasing gravity takes effect. In this circumstance, mass loss can only be established if a segregation can occur in which denser concentrations of mass fall back toward the disk plane, while the interspersed lower density gas (in which the line-driving force per unit mass is larger) continues to be accelerated outward by the radiation force. If this separation were only required to occur in the subcritical part of the flow, gas pressure effects might then act to smooth the density profile, thereby preventing the development of unstable behaviour. In practice, the radiation force term continues to be at a disadvantage with respect to gravity out to greater heights in all our models where the disk is the only source of radiation.

A critical aspect that facilitates the unsteady behaviour is the multi-dimensional character of the flow. In one dimension, it is likely that the increase in gravity with height would prevent an outflow being established at all in the case of a sub-Eddington disk. However, in two dimensions, streamlines can merge laterally, with the result that higher density

regions, in which the radiation force per unit mass and acceleration is reduced, are created alongside lower density gas that can be more readily accelerated to form the outflow. The contrast between a nearly planar flow from a disk and a spherical flow from a star is relevant here; the effects of streamline convergence would be reduced by geometric dilution in the latter.

We are certainly not the first to appreciate the significance of the increase in effective gravity with height for disk winds. For example, in their essentially one-dimensional treatment, Vitello & Shlosman (1988) dealt with the problem by deriving an ionization structure for the wind which ensured the radiation force tracked the rising gravity term. In contrast, we take the view that unsteady behaviour is likely to be a natural characteristic of disk winds and therefore see no need to condition our calculations to eliminate it.

Given the inherent instability present in the outflow, it is not surprising that our models show complex behaviour. All that is required to excite such behaviour are modest perturbations. These will arise in our models for several reasons related to the physics of the problem. For example, our initial conditions are not a perfect equilibrium state – rather, small radial pressure gradients excite both radial and vertical oscillations of the disk that can seed perturbations in the outflow. Vertical oscillations of the disk continue to be driven as dense material falls back onto the disk from the flow. In fact, the tendency of pressure-supported disks to undergo vertical oscillations (e.g., Cox, & Everson 1980; Lin, Papaloizou, & Savonije 1990) may ensure the flow will never reach a steady state. In addition to these small amplitude perturbations associated with the lack of perfect hydrostatic equilibrium in the initial state, there are large amplitude velocity perturbations associated with the transients generated during the establishment of the outflow. Finally, there is considerable velocity shear between the dense disk wind and the lower density fast stream defining the upper envelope of the flow. There is evidence in our simulations that this shear gives rise to Kelvin-Helmholtz instabilities.

It is well-known that even 1D radiation-driven stellar winds are subject to powerful instabilities (OCR). It is plausible this instability will be present in radiation-driven disk winds also, although the instability tends to produce strong shocks perpendicular to the outflow which we do not observe in our simulations. Even without these (as described above) there are other physical effects that will in any case lead to complex, unsteady flow.

A related and important feature of our calculations is that the addition of a strong radial component to the radiation field associated with a bright central star ‘organizes’ the flow into a steady state. The effect is almost certainly caused by the fact that the streamlines near the surface of the disk will be directed outwards of the purely vertical by the added stellar radiation. Thus, the effective gravity along the streamlines no longer increases, and the mechanism of the unsteady behavior (that gravity exceeds the radiation force at some distance from the disk) no longer operates.

Empirically, we have seen that, in the luminosity domain where the disk wind is robust, a CS half as luminous as the disk ( $x \simeq 0.5$ ) is sufficient to make this difference.

## 5.2 Application to CV

Our present calculations have been motivated by and designed for the case of winds from CV. We now consider whether the dynamical structures and mass loss rates predicted by them are likely to be appropriate.

The primary evidence for the existence of winds in CVs is contained within ultraviolet observations of high-state non-magnetic systems (dwarf novae in outburst and nova-like variables). In low inclination non-eclipsing systems, the profiles of the stronger resonance lines include broad blueshifted absorption indicating outflow. The maximum expansion velocities inferred are on the order of a few thousand  $\text{km s}^{-1}$  and are thus comparable with the typical white dwarf escape velocity. A point of contrast between the line profile shapes seen in OB stars and CVs, is that deepest absorption is achieved near terminal velocity in the former, but near line centre in the latter (e.g. see data presented by Prinja & Rosen 1995). In high inclination eclipsing systems, the P Cygni absorption is replaced by broad high contrast line emission. The order of magnitude decrease in expansion speed with respect to a spherically-symmetric MS star wind ( $v_\infty \sim 1500 \text{ km s}^{-1}$ ; Howarth & Prinja 1989) is particularly significant. Associated with the changed mass flux and the restricted opening angle of the outflow is a density that can be up to  $\sim 100$  times higher than would be expected of a spherically-symmetric stellar wind – the efficiency of H I line emission would presumably rise by a still larger factor. All of these effects are substantive changes in the right direction, suggesting that a radiation-driven disk wind model for massive YSOs is worth further investigation.

Adopting a mass accretion rate consistent with values inferred from observations of high-state CV (i.e.  $\dot{M}_a \sim 3 \times 10^{-8} M_\odot \text{ yr}^{-1}$ , e.g. Warner 1987) leads us to consider a qualitative comparison of model 3 with observation. This model is characterised by complex dense flow near the equatorial plane bounded by a fast stream (see Figure 10a). Typical velocities in these two components are  $\sim 200 \text{ km s}^{-1}$  and  $\sim 2000 \text{ km s}^{-1}$  respectively. On viewing such an object at low inclination, we would expect to see high-velocity blueshifted absorption due to the fast stream combined with a substantial low-velocity absorption component originating in the more slowly churning equatorial gas. At high inclinations the low-velocity component should still be apparent in absorption, while the high velocity gas will appear in emission if it is no longer seen in projection against the bright inner disk. Hence both at low inclination and at high inclination, the kinematic structure of the model outflow appears to be capable of matching the characteristics indicated by observation.

Clearly, it will be appropriate to confirm qualitative im-

pression of agreement by carrying out detailed line profile synthesis based on these models. When this is undertaken, it may well be appropriate to think again about the boundary condition currently imposed at the surface of the white dwarf. In the interests of simplicity we have thus far ignored the possibility that there may yet be a significant component of boundary layer emission between the disk and star, and have not allowed any mass loss from the star itself. In a crude way, the  $x = 1$  models give some idea as to what impact the presence of a hot white dwarf and non-planar boundary layer might have. Mass loss from the star could very well add significantly to the total column contained within the fast stream – particularly if the star is allowed to rotate at a significant fraction of break-up. These are, however, issues that amount to the introduction of further free parameters that should be faced in the future, rather than taken on board now, at the outset.

If, as our models suggest, there is an equatorial zone of complex time-dependent flow, there are consequences of this that may be directly observable. We find the flow varies on timescales of order of the local orbital period, i.e. a few tens of seconds in the vicinity of a white dwarf. If this behaviour is present in real systems and gives rise to a granularity on a spatial scale not too small compared with the total extent of the effective resonance line-forming region, we can expect the low velocity absorption component to vary on this timescale. This prediction is just within the realms of testability using highly time resolved HST spectra. The effect may be looked for both in high and low inclination systems

We now come to the question of the comparison between model and observed mass loss rates. We find for  $\dot{M}_a \sim 3 \times 10^{-8} M_\odot \text{ yr}^{-1}$  that the mass loss rate in the wind is  $5 \times 10^{-12} M_\odot \text{ yr}^{-1}$  for  $\alpha = 0.6$ , rising to almost  $1 \times 10^{-10} M_\odot \text{ yr}^{-1}$  for  $\alpha = 0.8$  (see Table 2 and Figure 8). The reason for this sensitivity is that the higher value of  $\alpha$  causes the force multiplier to achieve its maximum value earlier in the flow. Observational lower limits based on profile fitting uncorrected for unknown ion abundances span much the same range (e.g. Drew 1997, Prinja & Rosen 1995). Estimates based on ionization models require  $\dot{M}/\dot{M}_a$  in the region of a few percent (Hoare & Drew 1993). In view of our expectation that the present calculations are liable to underestimate the wind mass loss, this initial comparison is very encouraging indeed. However, it is also true that there is yet much work to be done to determine internally consistent choices for the parameters  $k$  and  $\alpha$  that control the radiation force multiplier. Thus far we have just used values typical for single hot stars.

Lastly, we note that the mass loss is modelled as showing a sharp cut-off as the product of the total luminosity and maximum force multiplier decreases below a critical value. Presently this is twice the Eddington limit, and translates at small  $x$  and  $\alpha = 0.6$  into  $\dot{M}_a \simeq 10^{-8} M_\odot \text{ yr}^{-1}$ . There is a parallel to this behaviour in ultraviolet observations of dwarf novae undergoing outburst, where it has been noted that P-Cygni absorption features are apt to disappear very suddenly as the decline from maximum light begins. A good example of this was seen early in a decline of SU UMa (Woods,



Drew & Verbunt 1990), when a factor of 2 decrease in the UV continuum erased what had been prominent blueshifted absorption in CIV 1549Å and other lines at maximum. Another aspect of this is that different systems apparently present very different levels of mass loss, despite the expectation that the high state viscosity, and hence mass accretion rates, cannot vary by more than a factor of a few (e.g. compare and contrast the weak blueshifted absorption features in SS Cyg, during outburst, with the extremely strong features in RW Sex, a nova-like variable, Prinja & Rosen 1995). Ultimately this effect will provide a useful quantitative calibration of radiation driven disk wind models against observation. For the timebeing, it is again encouraging that the cut-off occurs at a mass accretion rate comparable with those believed to be attained during outburst.

### 5.3 General scaling

The models presented in this paper have all been calculated for white dwarf accretion disks. We show below how our models might be scaled to produce guideline mass loss rates and expansion velocities for other applications.

We introduce a set of primed dimensionless variables. First, it is natural to scale lengths to the stellar radius,  $r_*$ :

$$r = r' r_* \quad (15)$$

and define the unit time  $\tau = \sqrt{\frac{r_*^3}{GM_*}}$ , as earlier, such that

$$t = t' \tau. \quad (16)$$

The unit velocity is accordingly  $v_o = \sqrt{\frac{GM}{r_*}}$ . For the white dwarf case this is 3017 km s<sup>-1</sup>. Translational velocity and the sound speed then become:

$$\mathbf{v} = \mathbf{v}' v_o \quad (17)$$

and

$$c_s = c'_s v_o \quad (18)$$

In our models,  $c'_s = 4.6 \times 10^{-3}$ . The Eddington factor expressed in terms of just the disk luminosity is

$$\Gamma = \frac{\sigma_e \dot{M}_a}{8\pi c r_*} \quad (19)$$

where  $\sigma_e$  is the Thompson scattering cross-section divided by the mass of the hydrogen atom.

Using these new variables, the equation of motion can be rewritten in the dimensionless form:

$$\rho' \frac{D\mathbf{v}'}{Dt'} = -c'_s{}^2 \nabla(\rho') + \rho' \frac{1}{r'^2} + \frac{6\rho'\Gamma}{\pi} (\mathbf{f}_D(x) + \mathbf{f}_D^l(x, M) + \mathbf{f}_*(x) + \mathbf{f}_*^l(x, M)), \quad (20)$$

where the scaling to a dimensionless density via  $\rho = \rho' \rho_o$  is trivial. This equation has three parameters:  $c'_s$ ,  $\Gamma$ ,  $x$ , and depends on one dimensionless function – the locally-determined force multiplier,  $M(t)$ . We can approximate and hence simplify this somewhat. First, for many cases of interest, the electron scattering terms will be of minor importance compared to the line acceleration terms and so may be neglected. Second, we may conclude from the empirical absence of a dependence upon  $x$  in the relations between total luminosity and either mass loss rate or outflow velocity (Figs. 8b & 9b) that the disk and CS driving terms can be combined to yield:

$$\rho' \frac{D\mathbf{v}'}{Dt'} \simeq -c'_s{}^2 \nabla(\rho') + \rho' \frac{1}{r'^2} + \frac{6\rho'}{\pi} (1+x) \Gamma M(t) f'(r, \theta) \quad (21)$$

wherein  $f'(r, \theta)$  is a factor encompassing all the geometric aspects of the radiation force calculation. A priori it was not possible to assume that the dynamics might be reducible to such a form.

It only remains to provide a scaling to allow mass loss rates to be estimated for other applications. This can be extracted from the definition of the dimensionless Eddington factor,  $\Gamma$ , in that we can define a fiducial mass time derivative such that  $\dot{M}_o = 8\pi c r_* / \sigma_e$ . The mass loss rate will then scale as

$$\dot{M}_w = \dot{M}'_w \dot{M}_o \quad (22)$$

In Figs. 8b and 9b we provide as alternate ordinates the quantities  $\dot{M}'_w$  and  $v'_r$  in order to facilitate rescaling of our results to other contexts for which  $\dot{M}_o$  and  $v_o$  can be estimated.

### 5.4 Other astrophysical applications

Although the models presented in this paper have been motivated primarily by observations of CVs, there are clearly other astrophysical systems to which our results may be relevant. Here we discuss just two such cases: accretion disks associated with active galactic nuclei (AGN), and massive young stellar objects.

The presence of broad, blueshifted absorption lines in quasar spectra (Osterbrock 1989) is often interpreted as evidence for a line-driven disk wind. Recently, Murray et al (1995) have constructed dynamical models for such winds

based on the solution of the one-dimensional (radial) equation of motion subject to certain assumptions about how the gas is loaded onto radial streamlines via vertical motions. It is not clear whether these assumptions lead to a good representation of the streamlines in a fully two-dimensional solution such as presented here.

The bulk of the radiative flux in quasars comes from or near the central source, implying our models with very large values for the parameter  $x$  should be most appropriate to these systems. The most extreme value of  $x$  we have considered is 10 (model 14). In it, we find strongly radial flow confined to angles of less than 30 degrees from the disk mid-plane with little time-dependence. However, the radiation from the central source in the AGN case is very much harder than that produced locally in the disk and, as the former increasingly dominates over the latter with increasing height above the disk photosphere, it is plausible that the force multiplier would become a function of position to reflect this (see Vitello & Shlosman 1988, Murray et al. 1995). This is not an effect that our present models include. At least a simplified treatment of the photoionization and recombination of the wind material is required before the two-dimensional structure of quasar winds can be examined self-consistently.

In the case of high mass young stellar objects, e.g. the BN-type objects and Herbig Be stars, photoionization effects are not an overriding concern in that the literature already contains force multiplier parameters designed for the appropriate effective temperature range. A more fundamental issue is the nature and extent of their circumstellar disks, as this cannot yet be said to have been defined compellingly. That disks of some kind are present has been entertained by many (Simon et al. 1985; Hamann & Persson 1989; Chandler, Carlstrom & Scoville 1995 – to mention a few). A major phenomenological challenge of these objects is the dynamical origin of their often extremely bright, yet modestly velocity-broadened ( $\Delta v_{FWHM} \sim 200 \text{ km s}^{-1}$ ) hydrogen line emission. If, like classical T Tau stars, these objects are in an active accretion phase, the ratio of stellar to disk luminosity may not be too extreme. For instance, an early B star accreting at a rate of  $\sim 10^{-6} M_{\odot} \text{ yr}^{-1}$  would be described by  $x \sim 100$ . Since, for  $x \gtrsim 10$ , the disk's light is dominated by the reprocessed component, there is no substantive difference between  $x = 10$  and any higher value of  $x$ . Thus, our model 14 with  $x = 10$  may again be crudely indicative of the outflow geometry we might expect for such systems. The expectation is therefore that the outflow would be equatorial and steady.

A more interesting point, however, is that the flow is very likely to be very much more dense and significantly less rapidly expanding than a conventional early-type stellar wind. Specifically, the effective Eddington number ( $M_{max}L/L_{edd}$ ) for an early B star is likely to be in the region of 20 or so, while the scaling variables,  $v_o$  and  $\dot{M}_o$  (section 5.3), are respectively  $\sim 500 \text{ km s}^{-1}$  and  $\sim 0.01 M_{\odot} \text{ yr}^{-1}$ . These numbers combine with the results in Figs. 8b and 9b to yield mass loss rates estimates in excess of  $10^{-8} M_{\odot} \text{ yr}^{-1}$  and maximum expansion velocities of  $\sim 500 \text{ km s}^{-1}$  (i.e.  $v'_r \sim 1$ ). This amounts to an order of magni-

tude increase in  $\dot{M}_w$  and a factor of a few decrease in expansion speeds with respect to a spherically symmetric MS star wind ( $\dot{M}_w \sim 10^{-9} M_{\odot} \text{ yr}^{-1}$ ,  $v_{\infty} \sim 2000 \text{ km s}^{-1}$ ; Howarth & Prinja 1989). The net impact of both these differences and the restricted opening angle of the outflow could be to raise the density, with respect to a normal MS stellar wind, by a factor of a few tens and the efficiency of H I line emission by a factor of 100–1000 perhaps. All of these effects are substantive changes in the right direction, suggesting that a radiation-driven disk wind model for massive YSOs is worthy of further investigation.

## 5.5 Limitations of the present models

There are a number of limitations of the present analysis which are worthy of mention and further investigation.

Perhaps the most important relate to the approximations adopted here to represent the radiation force. We have already discussed, in section 4.4, the tests we have performed to check the sensitivity of our models to an improved representation of the general line-driving force in a multidimensional wind. Based on these tests, we conclude it is unlikely that the major results of this paper (for example, the two-dimensional geometry of line-driven winds from disks, or the existence of unsteady behavior in low luminosity systems) will change with a formalism which includes all terms in the radiation force on lines. However, quantities such as the mass loss rate and terminal velocity reported here should only be considered accurate to factors of a few. Here, we also wish to point out that in a rotating wind there are azimuthal forces even in axisymmetry (because not all terms in the velocity gradient projected along the line of sight  $dv_i/dl$  are symmetric in  $\phi$ , see equations 8 and A2); these forces may change the angular momentum of the gas and effect the dynamics of the wind. While we expect such effects to be small, we have yet to study them in detail. We shall report the results of our calculations using a more general treatment of the radiation force on lines in a two-dimensional, rotating wind in a future communication.

Of course, a more fundamental concern is whether the Sobolev approximation should even apply in principle to the multidimensional and time-dependent flows considered here. In adopting the Sobolev approximation, we have ignored non-local radiative transfer effects. Because the velocity field in some of the models reported here is neither monotonic nor steady, non-local effects such as shadowing can be expected to affect the solutions. A proper study of these effect requires the use of algorithms for multidimensional transport of line radiation in a rotating wind, which is beyond the scope of the present work. However, it may be anticipated that the inclusion of shadowing would have a similar effect to increased  $x$  for the reason that shadowing should mostly reduce the driving of the slow equatorial component and have little impact on the relatively well-organized fast boundary stream.

Other effects which bear further investigation are the inclusion of mass loss from the central star. This however requires a realistic prescription for the properties of the radiation field and gas flow in the interaction region (boundary layer) between the CS and accretion disks. Since magnetic fields are likely to be central to the production of angular momentum transport in accretion disks (Balbus & Hawley 1997), it would also be fruitful to consider the effect of a global magnetic field anchored in the disk on the properties of the wind.

Finally, we have considered the two-dimensional structure of winds assuming an isothermal equation of state. Thermal pressure effects can be expected to be important only in the subsonic acceleration zone, which we find is generally small in spatial extent. Nevertheless, we have not modeled the transition between the optically-thick (and therefore adiabatic) gas inside the disk, and the optically thin wind above. In principle, the radial variation in the internal structure of the disk caused by the radial variation in temperature might affect conditions at the base of the wind. This inadequacy is not so serious given that the main seat of the outflow is the relatively small area of the innermost disk ( $r \lesssim 2r_*$ ).

Clearly dynamical models which consider the internal magnetohydrodynamics of an optically thick, turbulent accretion disk (Brandenburg et al 1995; Stone et al 1996) and radiation pressure on spectral lines in the wind region above the disk are the most appropriate description of real disks; such models await future studies.

## 6 CONCLUSIONS

Using numerical methods to solve the two-dimensional, time-dependent equations of hydrodynamics, we have studied radiation driven winds from luminous accretion disks. In so doing we have accounted for the radiation force mediated by spectral lines using a generalized multidimensional formulation of the Sobolev approximation. Our primary conclusions are the following.

(1) We find radiation driven winds from luminous accretion disks are intrinsically unsteady: the outflow consists of large amplitude density and velocity fluctuations, with some regions of dense material undergoing infall. This behavior is rooted in the difference in the variation with height of the vertical component of gravity and the radiation force. Since the former increases, it grows until it overwhelms the radiation force, causing high density material (in which the radiation force per unit mass is low) to stall. Despite the fact that instantaneous values in the wind are variable, time-averaged values are constant.

(2) The contribution of a strong radial component to the driving radiation field from a bright central star serves to ‘organize’ the outflow into a steady state. Very bright

central stars produce steady transsonic disk winds. Moreover, the region producing unsteady outflow is reduced as the luminosity of the disk is increased.

(3) Regardless of whether the flow is steady or unsteady, we find the time-averaged geometry of the flow typically consists of a dense, nearly equatorial, low velocity flow confined to angles within  $30^\circ$  to  $45^\circ$  of the equatorial plane, bounded by a lower density, high velocity flow in a channel at larger angles. In the absence of a wind directly from the central star the gas density in the polar regions is so low as to be of no dynamical or observable significance. Most of the mass loss occurs within a few stellar radii of the central star.

(4) The geometry of the radiation field is a major factor in controlling the geometry of the outflow. Increasing the luminosity of the star at a fixed disk luminosity produces a radial wind confined to smaller regions near the equatorial plane. Conversely, increasing the disk luminosity at a fixed stellar luminosity produces a more polar outflow.

(5) The total mass loss rate and terminal velocity in the wind depends on the total luminosity of the star plus disk system, but is insensitive to the outflow geometry or whether the wind is steady or unsteady. No outflow is produced if the effective luminosity of the disk (that is, the luminosity of the disk times the maximum value of the force multiplier associated with the line-driving force) is less than the Eddington limit. Above the Eddington limit, the mass loss rate in the wind scales with the effective luminosity as a power law with index of about 1.5. The effective luminosity can be increased either by increasing the accretion rate in the disk, or by increasing the brightness of the central star. The ratio of the mass loss rate in the wind to the accretion rate increases sharply, reaching a few percent for the most luminous disks considered.

This study has been motivated primarily by high resolution spectroscopic observations of winds from disks in CV systems. The overall structure of disk winds revealed by our calculations, i.e. a dense equatorial wind with a fast polar outflow, appear to be in agreement with the kinematics inferred for real systems. Furthermore, the magnitude of the mass loss rates obtained on adopting a force multiplier parameterisation known to be applicable to OB stars overlaps the range that has been deduced from observation. We plan more detailed comparison of line profiles computed from our models with observational data in the future. Future applications also include high mass YSOs with circumstellar disks (in which case outflow from the central star must also be allowed), and AGN (in which case photoionization of the wind by the central source must be taken into account).

**Acknowledgments:** This research has been supported by a research grant from PPARC, and by NASA through HST grant GO-6494. Computations were performed at the Pittsburgh Supercomputing Center.

**APPENDIX A: CALCULATION OF THE RADIATION FIELD FROM DISK AND CENTRAL STAR**

We use a spherical polar coordinate system with an origin at point C, the center of the CS. Colatitude ( $\theta$ ) is measured from the rotation axis of the disk, and azimuth ( $\phi$ ) is measured from a plane perpendicular to the disk plane, containing the point C and a point W above the disk (see Figure A.1). We define the location of a wind point, W, and a disk point, D, by the co-ordinates  $(r, \theta, 0^\circ)$  and  $(r_D, 90^\circ, \phi_D)$  respectively. The distance between D and W then is

$$d_D = (r_D^2 + r^2 - 2r_D r \cos \beta_D)^{1/2}, \quad (\text{A1})$$

where  $\beta_D$  is the angle WCD and  $\cos \beta_D = \sin \theta \cos \phi_D$ . The direction D toward W can be defined by the unit vector  $\hat{n} = (n_r, n_\theta, n_\phi)$ . Using the coordinates of points D and W,

$$n_r = \frac{r - r_D \sin \theta \cos \phi_D}{d_D}; \quad n_\theta = \frac{r_D \cos \theta \cos \phi_D}{d_D}; \quad n_\phi = \frac{r_D \sin \phi_D}{d_D}. \quad (\text{A2})$$

The intensity of an  $\alpha$ -disk at point D is (e.g., Pringle 1981)

$$I_D(r_D) = \frac{3GM_* \dot{M}_a}{8\pi^2 r_D^3} \left( 1 - \left( \frac{r_*}{r_D} \right)^{1/2} \right), \quad (\text{A3})$$

where  $M_*$  and  $r_*$  are the mass and radius of the central star,  $\dot{M}_a$  is the accretion rate through the disk (Shakura & Sunayev 1973). The total luminosity of an  $\alpha$ -disk is

$$L_D = \frac{GM_* \dot{M}_a}{2r_*}. \quad (\text{A4})$$

In the presence of a luminous CS, the intensity radiated by an optically-thick  $\alpha$ -disk changes due to heating of the disk by the CS radiation. To calculate this illumination effect, it is convenient to describe the location of the CS surface point S in a spherical polar coordinate system  $(R, \Theta, \Phi)$  in which the origin is at the point D. The colatitude  $\Theta$ , is now measured from the DC axis and the azimuth  $\Phi$ , is measured from the plane perpendicular to the disk surface that contains both the points D and C. Expressing the central star luminosity in  $L_D$  units

$$L_* = x L_D = x \frac{GM_* \dot{M}_a}{2r_*}. \quad (\text{A5})$$

and assuming that the CS surface is isothermal, the CS intensity then is

$$I_* = \frac{L_*}{4\pi^2 r_*^2} = x \frac{GM_* \dot{M}_a}{8\pi^2 r_*^3}. \quad (\text{A6})$$

The stellar energy absorbed per unit time by a surface element of the disk is

$$\frac{dE}{dAdt} = I_* \int_{-\pi/2}^{\pi/2} \int_0^{\Theta_{max}} \cos \Phi \sin^2 \Theta \, d\Theta d\Phi = I_* (\Theta_{max} - \sin \Theta_{max} \cos \Theta_{max}), \quad (\text{A7})$$

where,  $\sin \Theta_{max} = r_*/r$ .

Assuming that the disk reemits the absorbed energy locally as a black body, the disk intensity due to irradiation can be written as



At the point W, the radiation flux due to the stellar surface element between  $(\theta_s, \theta_s + d\theta_s)$  and  $(\phi_s, \phi_s + d\phi_s)$  is

$$d\mathcal{F}_* = \frac{I_* \sin \theta_s (r \cos \theta_s - r_*)}{d_*^3} r_*^2 d\theta_s d\phi_s. \quad (\text{A12})$$

## APPENDIX B: CALCULATION OF THE RADIATION FORCE FROM DISK AND CENTRAL STAR

The radiation force due to electron scattering, per unit mass, contributed by the disk surface element along  $\hat{n}$  is

$$d\mathbf{F}_D^{\text{rad},e} = \hat{n} \frac{\sigma_e}{c} d\mathcal{F}_D \quad (\text{B1})$$

where  $\sigma_e$  is the mass scattering coefficient of free electrons. We assume that the mean mass of the particle is equal to the proton mass,  $m_p$ . Thus  $\sigma_e = \sigma_T/m_p$ , where  $\sigma_T$  is the Thomson cross section.

Using equations A9 and A10 we obtain from equation B1 the radiation force per unit mass from the total disk surface acting a point W: namely,

$$\mathbf{F}_D^{\text{rad},e} = \frac{3\sigma_e G}{4\pi^2 c} \frac{M_* \dot{M}_a}{r_*^3} \mathbf{f}_D(r', \theta) \quad (\text{B2})$$

where  $\mathbf{f}_D$  is the vector-valued integral

$$\mathbf{f}_D(r', \theta) = \int_{\phi_l}^{\phi_u} \int_{r'_i}^{r'_o} \hat{n} \frac{r' \cos \theta}{r_D'^2 d_D'^3} \left( 1 - \left( \frac{1}{r_D'} \right)^{1/2} + \frac{x r_D'^3}{3\pi} \left( \arcsin \frac{1}{r_D'} - \frac{1}{r_D'} \left( 1 - \left( \frac{1}{r_D'} \right)^2 \right)^{1/2} \right) \right) dr_D' d\phi_D, \quad (\text{B3})$$

in which the primed quantities are expressed in  $r_*$  units. The integration limits,  $r'_i$ ,  $\phi_l$ , and  $\phi_u$  are functions of position because of the need to account for the shadowing of the disk by the CS. The upper limit on the radial integration is always the outer radius of the disk,  $r'_o$ . The integral with respect to  $\phi$  is calculated assuming symmetry about the  $\phi = 0$  plane.

Using the CAK formalism (see §2) the radiation force per unit mass, due to spectral lines along  $\hat{n}$ , contributed by a disk surface element is

$$d\mathbf{F}_D^{\text{rad},l} = \hat{n} \frac{\sigma_e}{c} d\mathcal{F}_D M(t), \quad (\text{B4})$$

where  $M(t)$  is the force multiplier. Following the analogy with  $F_{Di}^{\text{rad},e}$ , the total radiation force due to lines from the disk is

$$\mathbf{F}_D^{\text{rad},l} = \frac{3\sigma_e G}{4\pi^2 c} \frac{M_* \dot{M}_a}{r_*^3} \mathbf{f}_D^l(r', \theta, ), \quad (\text{B5})$$

where  $\mathbf{f}_D^l$  is the vector-valued integral

$$\mathbf{f}_D^l(r', \theta) = \int_{\phi_l}^{\phi_u} \int_{r'_i}^{r'_o} \hat{n} \frac{r' \cos \theta}{r_D'^2 d_D'^3} M(t) \left( 1 - \left( \frac{1}{r_D'} \right)^{1/2} + \frac{x r_D'^2}{3\pi} \left( \arcsin \frac{1}{r_D'} - \frac{1}{r_D'} \left( 1 - \left( \frac{1}{r_D'} \right)^2 \right)^{1/2} \right) \right) d\phi_D dr_D'. \quad (\text{B6})$$

The radiation force due to electron scattering from a stellar surface element is

$$d\mathbf{F}_*^{rad,e} = \hat{m} \frac{\sigma_e}{c} d\mathcal{F}_* \quad (\text{B7})$$

and using equations A6 and A12, the angle-integrated force becomes

$$\mathbf{F}_*^{rad,e} = \frac{3\sigma_e G}{4\pi^2 c} \frac{M_* \dot{M}_a}{r_*^3} \mathbf{f}_*(r, \theta), \quad (\text{B8})$$

where  $\mathbf{f}_*$  is the vector-valued integral

$$\mathbf{f}_*(r, \theta) = x \int_0^{\theta_u} \int_{\phi_i}^{\phi_o} \hat{m} \frac{\sin \theta_s (r \cos \theta_s - r_*) r_*^2}{3d_*'^3} d\theta_s d\phi_s, \quad (\text{B9})$$

By analogy with equation B2, the stellar component of the radiation force due to lines is

$$\mathbf{F}_*^{rad,l} = \frac{3\sigma_e G}{4\pi^2 c} \frac{M_* \dot{M}_a}{r_*^3} \mathbf{f}_*^l(r, \theta) \quad (\text{B10})$$

where

$$\mathbf{f}_*^l(r, \theta) = x \int_0^{\theta_u} \int_{\phi_i}^{\phi_o} \hat{m} \frac{\sin \theta_s (r \cos \theta_s - r_*') r_*'^2}{3d_*'^3} M(t) d\theta_s d\phi_s, \quad (\text{B11})$$

Finally, the total radiation force per unit mass acting on a particle at point W is

$$\mathbf{F}^{rad} = \mathbf{F}_D^{rad,e} + \mathbf{F}_D^{rad,l} + \mathbf{F}_*^{rad,e} + \mathbf{F}_*^{rad,l} \quad (\text{B12})$$

or using the vector-valued integrals B3, B6, B9 and B11:

$$\mathbf{F}^{rad} = \frac{3\sigma_e G}{4\pi^2 c} \frac{M_* \dot{M}_a}{r_*^3} (\mathbf{f}_D + \mathbf{f}_D^l + \mathbf{f}_* + \mathbf{f}_*^l). \quad (\text{B13})$$

### APPENDIX C: THE RADIATION FORCE DUE TO LINES FOR SPECIAL CASES.

To calculate the radiation force from the CS we consider the simple case where we assume that  $Q$  is dominated by terms associated with the radial component of the velocity

$$Q = \frac{dv_r}{dr} n_r^2 + \frac{v_r}{r} (n_\theta^2 + n_\phi^2) = \frac{dv_r}{dr} \mu^2 + \frac{v_r}{r} (1 - \mu^2), \quad (\text{C1})$$

where  $\mu = \hat{m} \cdot \mathbf{v} = \frac{r - r_* \cos \theta}{d_s}$  (see Rybicki & Hummer 1983). If we further assume  $\mu = 1$ , i.e. that the star is a point source, then

$$Q = \frac{dv_r}{dr}. \quad (\text{C2})$$

This is exactly the case considered by CAK. As we described in §2, an advantage of this approximation is that, in the calculation of the radiation line force due to the whole star, we can move a time dependent, velocity factor outside the integral in equation B11:

$$\mathbf{f}_*^l(r, \theta) = k \left( \sigma_e \rho v_{th} \left| \frac{dv_r}{dr} \right|^{-1} \right)^{-\alpha} \left[ \frac{(1 + \tau_{max})^{(1-\alpha)} - 1}{\tau_{max}^{(1-\alpha)}} \right] \int_0^{\theta_u} \int_{\phi_i}^{\phi_o} \hat{m} \frac{\sin \theta_s (r \cos \theta_s - r_*) r_*^2}{3d_*^3} d\theta_s d\phi_s. \quad (\text{C3})$$

Thus we need to calculate the integral only once at the beginning of the hydrodynamic calculations and update the radiation line force every time step only through  $\frac{dv_r}{dr}$ . However even in a purely radial wind, time-dependent calculations become very costly if we take into account a star with a finite disk (for example, see the Appendix of CAK, Pauldrach, Puls, Kudritzki 1986, Friend & Abbott 1986).

We also make use of an analogous major simplification of the disk radiation force. Assuming that the gradient of the velocity along the vertical direction is the dominant term, equation (8) reduces to

$$Q = \frac{dv_z}{dz} n_z^2, \quad (\text{C4})$$

where  $n_z = \frac{r' \cos \theta}{d'_D}$ . Numerically, this form of  $Q$  is constructed from its equivalent form in spherical coordinates:

$$Q = \left( \cos^2 \theta \frac{dv_r}{dr} + \sin^2 \theta \frac{1}{r} \left( v_r + \frac{dv_\theta}{d\theta} \right) + \sin \theta \cos \theta \left( \frac{v_\theta}{r} - \frac{1}{r} \frac{dv_r}{d\theta} \right) \right) \left( \frac{r' \cos \theta}{d'_D} \right)^2. \quad (\text{C5})$$

In this case, equation B6 can be expressed as

$$\mathbf{f}_D^l(r, \theta) = k \left( \sigma_e \rho v_{th} \left| \frac{dv_z}{dz} \right|^{-1} \right)^{-\alpha} \int_0^{\phi_u} \int_{r_i}^{r_o} \hat{n} \frac{r' \cos \theta}{r_D'^2 d_D'^3} \left( \frac{r' \cos \theta}{d'_D} \right)^{2\alpha} \left[ \frac{(1 + \tau_{max})^{(1-\alpha)} - 1}{\tau_{max}^{(1-\alpha)}} \right] \left( 1 - \left( \frac{1}{r'_D} \right)^{1/2} + \frac{x r_D'^2}{3\pi} \left( \arcsin \frac{1}{r'_D} - \frac{1}{r'_D} \left( 1 - \left( \frac{1}{r'_D} \right)^2 \right)^{1/2} \right) \right) d\phi_D dr'_D. \quad (\text{C6})$$

In the present form we still find the time-dependent  $\tau_{max}$  term within the integrand. Strictly, we can not move the factor within square brackets in front of the integral because  $\tau_{max}$  is dependent on line-of-sight and hence position on the disk plane. Therefore we make an approximation that  $n_z = 1$  as far as  $\tau_{max}$  is concerned. Introducing a new variable,  $\tau'_{max} = \sigma_e \rho v_{th} \left| \frac{dv_z}{dz} \right|^{-1} \eta_{max}$ , equation C6 can be rewritten

$$\mathbf{f}_D^l(r, \theta) = k \left( \sigma_e \rho v_{th} \left| \frac{dv_z}{dz} \right|^{-1} \right)^{-\alpha} \left[ \frac{(1 + \tau'_{max})^{(1-\alpha)} - 1}{\tau'_{max}^{(1-\alpha)}} \right] \int_0^{\phi_u} \int_{r_i}^{r_o} \hat{n} \frac{r' \cos \theta}{r_D'^2 d_D'^3} \left( \frac{r' \cos \theta}{d'_D} \right)^{2\alpha} \left( 1 - \left( \frac{1}{r'_D} \right)^{1/2} + \frac{x r_D'^2}{3\pi} \left( \arcsin \frac{1}{r'_D} - \frac{1}{r'_D} \left( 1 - \left( \frac{1}{r'_D} \right)^2 \right)^{1/2} \right) \right) d\phi_D dr'_D. \quad (\text{C7})$$

Now both the time-dependent factors appear outside the integral. Note that our approximation gives exactly the same result as equation C7 for  $\tau_{max} \rightarrow \infty$  because then the factors in square brackets are unity in both equations C6 and C7 (see equation 5). For  $\tau_{max} \rightarrow 0$ , equation C7 gives values lower than C6 because the integrand in equation C7 is smaller than the integrand in equation C6 by a factor  $(\frac{r' \cos \theta}{d'_D})^{2\alpha}$ . However for a given  $\eta_{max}$ ,  $\tau_{max} \rightarrow 0$  occurs when  $t$  is very small. Small  $t$  will mainly be associated with regions high above the disk where the gas density is low. Bearing in mind that a foreshortened disk element at low  $\frac{r' \cos \theta}{d'_D}$  contributes at low weight compared to an element with  $\frac{r' \cos \theta}{d'_D} \sim 1$ , we can see that equation C7 is quite a reasonable approximation of equation C6 even for  $\tau_{max} \rightarrow 0$ .



## REFERENCES

- Abbott D.C. 1982, ApJ, 259, 282
- Batchelor G.K. 1967, An Introduction to Fluid Mechanics (Cambridge: Cambridge University Press)
- Balbus, S.A., & Hawley, J.F., 1997, Rev. Mod. Phys., in press.
- Brandenburg A., Nordlund A., Stein R.F., Torkelsson U. 1995, ApJ, 446, 741
- Carroll B.W., Cabot W., McDermott P.N., Savedoff M.P., Van Horn H.M. 1985, ApJ, 296, 529
- Castor J.I., Abbott D.C., & Klein R.I. 1975, ApJ, 195, 157 (CAK)
- Chandler C. J., Carlstrom J. E., Scoville N. Z. 1995, ApJ, 446, 793
- Cox J.P., & Everson B.L. 1980, ApJSS, 52, 451
- Drew J.E. 1997, in *Accretion phenomena and related outflows*, eds. D. Wickramasinghe, L. Ferrario, G. Bicknell, ASP Conf. Sers, in press
- Friend D.B., Abbott D.C. 1986, ApJ, 311, 701
- Gayley K. G. 1995, ApJ, 454, 410
- Hamada T., Salpeter E.E. 1961 ApJ, 134, 683
- Hamann F., Persson S. E. 1989, ApJ, 339, 1078
- Hoare M.G., & Drew J.E. 1993, MNRAS, 260, 647
- Howarth I.D., Prinja R.K. 1989 ApJS, 69, 527
- Icke V. 1980, AJ, 85, 329
- Icke V. 1981, ApJ, 247, 152
- Knigge C., Drew J.E. 1997, ApJ, in press
- Lin, D.N.C., Papaloizou, J.C.B., & Savonije, G.J. 1990, ApJ, 364, 326
- Lucy, L.B., & Solomon, P. 1970, ApJ, 159, 879
- Mason, K.O., Drew J.E., Cordova F.A., Horne K., Hilditch R., Knigge C., Lanz L., & Meylan T. 1995, MNRAS, 274, 271
- Mundt R., Ray T.P. 1994, in *The nature and evolutionary status of Herbig Ae/Be stars*, eds. P.S. Thé, M. R. Pérez, E.P.J. van den Heuvel, ASP Conf.Sers. 62, 237
- Murray, N., Chiang, J., Grossman, S.A., & Voit, G.M. 1995, ApJ, 451, 498
- Owocki S.P., Castor J.I., Rybicki, G.B. 1988, ApJ, 335, 914
- Osterbrock, D.E., 1989, *Astrophysics of Gaseous Nebulae and Active Galactic Nuclei* (Mill Valley:University Science Books)
- Pauldrach A., Puls J., & Kudritzki R.P. 1986, A&A, 164, 86
- Pereyra N.A., Kallman T.R. Blondin J.M. 1997, ApJ, 477, 368
- Pereyra, N.A., 1997. Ph.D. thesis, University of Maryland.
- Prinja, R.K., & Rosen, R. 1995, MNRAS, 273, 461
- Pringle J.E. 1981, ARAA, 19, 137
- Proga, D., Drew, J.E., & Stone, J.M. 1997, in preparation.
- Puls, J., Owocki, S.P., & Fullerton, A. 1993, A&A, 279, 457
- Rybicki G.B., & Hummer D.G. 1978, ApJ, 219, 654
- Rybicki G.B., & Hummer D.G. 1983, ApJ, 274, 380
- Shakura N.I., Sunyaev R.A. 1973 A&A, 24, 337
- Simon M., Peterson D. M., Longmore A. J., Storey J. W. V., Tokunaga A. T. 1985, ApJ, 300, 32
- Stevens I.R., & Kallman T.R. 1990, ApJ, 365, 321
- Stone J.M., & Norman M.L. 1992, ApJS, 80, 753
- Stone J.M., Hawley J.F., Gammie C.F., & Balbus S.A. 1996, ApJ, 463, 656
- Vitello P.A.J., & Shlosman I. 1988, ApJ, 327, 680
- Warner B. 1987 MNRAS, 227, 23
- Warner B. 1995, *Cataclysmic Variable Stars*, (Cambridge: Cambridge University Press)
- Weymann R.J., Morris S.L., Foltz C.B., Hewett P.C. 1991, ApJ, 373, 23
- Woods J.A., Drew J.E., & Verbunt F. 1990, MNRAS, 245, 323